Earth Systems and Environment
https://doi.org/10.1007/s41748-026-01108-4

ORIGINAL ARTICLE

Urban Expansion Amplifies Hydro-Saline Processes and Infrastructure Vulnerability in an Arid Coastal City: A Long-Term, Field-Calibrated Remote-Sensing Assessment

Abazar M. A. Daoud[1,2] · **Mahmoud M. Kazem**[1,3] · **Tibor Novák**[4] · **Péter Rózsa**[1]

Received: 10 December 2025 / Revised: 21 February 2026 / Accepted: 24 February 2026

Abstract

In arid coastal environments, urban expansion alters land–water interactions, leading to increased soil salinity and moisture accumulation across urban landscapes. This study examines the spatiotemporal evolution of soil salinity and moisture, and land-use/land-cover (LULC) changes in Port Sudan, an arid coastal city that experienced rapid expansion from 2008 to 2024. The limited vegetation cover enables effective shortwave infrared (SWIR)-based assessment of salinity and moisture, facilitating multi-temporal analysis of LULC change and hydro-saline impacts. The findings demonstrate significant landscape transformation driven by urbanization, with built-up areas nearly doubling, substantial rangeland expansion, and a pronounced reduction in bare ground. These land-use transitions are accompanied by a marked inland expansion of salinity and moisture-affected areas, increasing from 8.12 to 40.36 km^2 and from 120.15 to 245.49 km^2, respectively, particularly within low-lying and reclaimed sabkha terrains. Urban growth exhibits strong correlations with hydro-saline intensification ($R^2 = 0.77$ and 0.82), as increased surface impermeability and disrupted drainage promote salt accumulation and subsurface water retention. Field observations in representative urban areas confirm that persistent hydro-saline ground conditions are linked to salt crust formation, sustained surface moisture, and progressive corrosion of building materials and foundations. Time-series forecasting indicates that continued urbanization is likely to further extend hydro-salinity-affected areas through 2040, with projections suggesting a substantial spatial increase under current development trajectories, although with uncertainty related to environmental variability and temporal resolution. Overall, this study presents a field-calibrated, earth observation-based framework that connects urban expansion with hydro-saline processes and related coastal infrastructure vulnerability, supporting risk-informed planning and management in arid coastal regions.

Highlights

- Salinity and Moisture indices successfully mapped across 16 years using multi-sensor datasets.
- Integrated remote sensing and VES-EC calibration for semi-quantitative salinity assessment.
- New calibrated SI threshold (110) derived from EC-RS regression and field evidence.
- Inland expansion of saline and moist soils is linked to rapid urbanization and surface modification.
- Predictive modeling shows saline-affected areas may exceed 150 km2 by 2040 without mitigation.

✉ Abazar M. A. Daoud
abazar.daoud@science.unideb.hu

Mahmoud M. Kazem
mahkazem99@gmail.com

Tibor Novák
novak.tibor@science.unideb.hu

Péter Rózsa
rozsa.peter@science.unideb.hu

[1] Department of Mineralogy and Geology, University of Debrecen, Egyetem Tér 1, 4032 Debrecen, Hungary

[2] Faculty of Earth Sciences, Red Sea University, Red Sea State, Port Sudan, Sudan

[3] Water Research Center, Red Sea University, Red Sea State, Port Sudan, Sudan

[4] Faculty of Agricultural and Food Sciences and Environmental Management, Institute of Agricultural Chemistry and Soil Science, University of Debrecen, 4032 Egyetem Tér 1, Debrecen, Hungary

Published online: 21 March 2026

Graphical Abstract

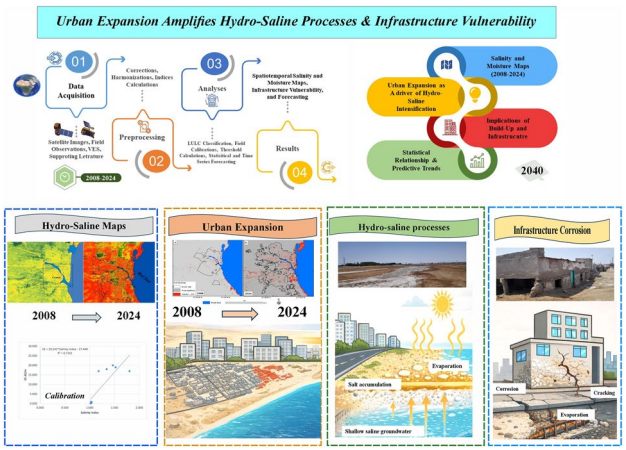

This graphical abstract demonstrates that rapid urban growth in Port Sudan, a dry coastal city, intensifies hydro-saline processes and increases infrastructure vulnerability. The study employs multiple data sources, including satellite imagery, MODIS land-use records, fieldwork, and electrical resistivity measurements, to provide a comprehensive assessment of soil salinity and moisture dynamics. All datasets are synchronized using atmospheric correction, temporal normalization, and surface reflectance standardization to ensure consistent analysis across 2008-2024. The analytical framework extracts salinity and moisture indicators (SI, NDMI/SMI, LST, LSE) and integrates them with land-use and land-cover (LULC) classification to quantify changes in built-up areas, bare ground, and rangeland. Calibration using 24 Vertical Electrical Sounding points and 6 solar salt sites establishes salinity (SI > 110) and moisture (SMI > 140) thresholds, enabling semi-quantitative interpretation of hydro-saline intensity. The resulting maps reveal an inland expansion of salinity and moisture from coastal sabkha into reclaimed and peri-urban areas, closely associated with increased impervious surfaces and modified drainage patterns. The graphical abstract shows strong correlations between urban expansion and increased salinity and moisture, confirming land-use transformation as a primary driver of hydro-saline intensification. ARIMA time-series modeling projects these trends through 2040, indicating continued expansion of built-up and salinity-affected areas. The final panel links these environmental changes to field observations of salt crusts, waterlogging, corrosion, cracking, and structural deterioration, emphasizing their impact on infrastructure stability.

Keywords Urbanization · Land use/land cover change · Salinity and moisture affected areas · Coastal infrastructure · Remote sensing · Corrosion · Time-series forecasting

1 Introduction

Arid coastal environments are increasingly affected by soil salinity and moisture accumulation, driven by the combined influence of shallow groundwater systems, marine intrusion, and climatic factors, such as high evaporation and limited precipitation (Meng et al. 2025). Natural hydro-saline processes, including tidal forcing, capillary rise, and groundwater–seawater mixing, are commonly intensified by anthropogenic pressures in rapidly urbanizing coastal zones (Heiss et al. 2022; Lorrain-Soligon et al. 2023; Morshed et al. 2016). Urban expansion, land reclamation, and surface sealing fundamentally transform land use and land cover (LULC), increasing impervious surfaces and disrupting natural drainage networks. These modifications alter soil–water interactions, reduce infiltration capacity, and promote subsurface water retention, particularly in low-lying and reclaimed coastal areas, thereby accelerating salt migration and accumulation in previously stable soils (Bashar and Uddin 2025; Hagage et al. 2024; Mazhar et al. 2022; Tarolli et al. 2024). As a result, hydro-saline degradation has emerged as a critical environmental challenge in many arid coastal cities worldwide (Eswar et al. 2021; Eyankware et al. 2025). Within this framework, urban growth acts as a primary driver linking LULC transformation to hydro-saline intensification, which in turn increases infrastructure vulnerability (Bhardwaj et al. 2019; Li et al. 2024; Mandal et al. 2025). Understanding the progressive cascade from land-use transformation through environmental degradation to structural deterioration relies on spatially explicit and temporally consistent observations that capture long-term spatiotemporal trends.Elevated soil salinity, combined with persistent moisture, presents significant risks to infrastructure stability from both engineering and urban sustainability

perspectives (Chen et al. 2022; Elsawy and Lakhouit 2020; Wijerathne et al. 2025). Soils rich in chloride and sulfate promote corrosion of reinforced concrete, weaken foundations, and reduce the service life of buildings, roads, and drainage systems (Saxena and Baghban 2023; Su et al. 2025). Moisture accumulation intensifies these effects by enabling capillary rise, salt crystallization, and chemically aggressive reactions within construction materials (Elena et al. 2024; Gökçe, 2024; Klein et al. 2022).

Remote sensing offers an effective framework for monitoring soil salinity, moisture dynamics, and LULC change across large spatial extents and extended time periods, particularly in regions where systematic ground-based monitoring is limited (Dey et al. 2025; Platonov et al. 2013). Advances in multispectral satellite sensors have enabled the application of shortwave infrared (SWIR)–based indices to characterize soil salinity and surface moisture conditions, especially in sparsely vegetated or barren landscapes typical of arid coastal environments (Lekka et al. 2024; Sahbeni et al. 2023; Salem and Jia 2024). While many remote sensing studies have addressed soil salinity and moisture in agricultural or natural settings, they often rely on vegetation-based indices in humid to semi-arid regions using moderate-resolution sensors, such as MODIS or Landsat (Gad et al. 2021; Masoud et al. 2019). Fewer investigations have focused on arid urban coastal environments. In such settings, SWIR-based indices derived from Landsat and Sentinel-2 data have proven effective for mapping saline soils and surface moisture under sparse vegetation conditions, particularly in desert and coastal sabkha landscapes (Bannari et al. 2018; Metternicht and Zinck 2003; Reul et al. 2020). When supported by targeted field calibration, these approaches provide robust tools for identifying hydro-saline affected zones, assessing environmental risk, and informing urban planning and engineering decisions. Despite this improvement, few studies have quantitatively integrated long-term LULC dynamics with hydro-saline processes and associated infrastructure impacts in arid coastal cities. Existing research often treats these components separately, lacks temporal continuity, or relies solely on remote sensing without field validation, limiting its ability to resolve causal relationships and long-term risk, particularly in the Red Sea region (Daoud et al. 2025; Hassani et al. 2020; Hawash et al. 2021). Port Sudan provides a compelling case study for addressing this gap. The city is characterized by near-zero vegetation cover, shallow saline groundwater, extensive sabkha deposits, reclaimed coastal land, and rapidly expanding urban development with limited drainage infrastructure (Daoud et al. 2025; Elsheikh and Elsayed 2015; Hawash et al. 2021). Over the past two decades, urban growth has increasingly encroached on saline-prone terrains, amplifying interactions among land-use change, hydro-saline processes, and infrastructure deterioration. These characteristics heighten the city's vulnerability and create favorable conditions for applying SWIR-based remote sensing techniques to distinguish soil salinity and moisture indicators and to examine their evolution in response to urban expansion.

This study aims to (i) analyze the spatiotemporal evolution of soil salinity and moisture in Port Sudan from 2008 to 2024, (ii) quantify LULC changes associated with rapid urban expansion, (iii) examine the spatial and statistical relationships between LULC transformation and hydro-saline intensification using field-calibrated remote sensing indices, and (iv) explore potential future trends through time-series analysis. By integrating high-resolution, multi-temporal satellite observations with ground-based verification and structural field evidence, this research establishes a comprehensive framework linking land-use transformation, subsurface hydro-saline processes, and infrastructure vulnerability in arid coastal regions.

2 Study Area

Port Sudan is situated on the western coast of the Red Sea in northeastern Sudan, between 19.30° and 19.70° N latitude, and 36.90° and 37.30° E longitude, covering approximately 1012 km^2 (Fig. 1). As the capital of Red Sea State and the temporary de facto capital of Sudan's main maritime gateway, the city has seen significant population growth and urban expansion over the past two decades (Brakman et al. 2025). This growth, driven by port-related economic activity, internal migration, and recent geopolitical factors, has led to the development of low-lying coastal plains, reclaimed land, and sabkha areas, often without adequate drainage or geotechnical planning.

Port Sudan's topography features a narrow coastal plain bordered by the Red Sea Hills, with elevations rising to the west. The area consists mainly of flat to gently undulating lowlands, interrupted by seasonal wadis and shallow depressions that affect surface runoff and groundwater recharge (Andrea Cattarossi et al. 2019). These features increase the city's vulnerability to flash floods, especially during irregular rainfall (Daoud et al. 2025). The region has a hyper-arid climate (BWh, Köppen classification), with mean annual rainfall below 100 mm, mostly in winter. Temperatures remain high year-round, with summer highs often above 40°C. Limited rainfall and high evaporation cause chronic water scarcity, and groundwater is typically saline and shallow, particularly near the coast (Harris et al. 2020; National Oceanic and Atmospheric Administration 2025).

The coastal plain of Port Sudan is composed mainly of unconsolidated Quaternary sediments, such as gravelly silty sands, fine sands, clays, coral reef limestone, and extensive

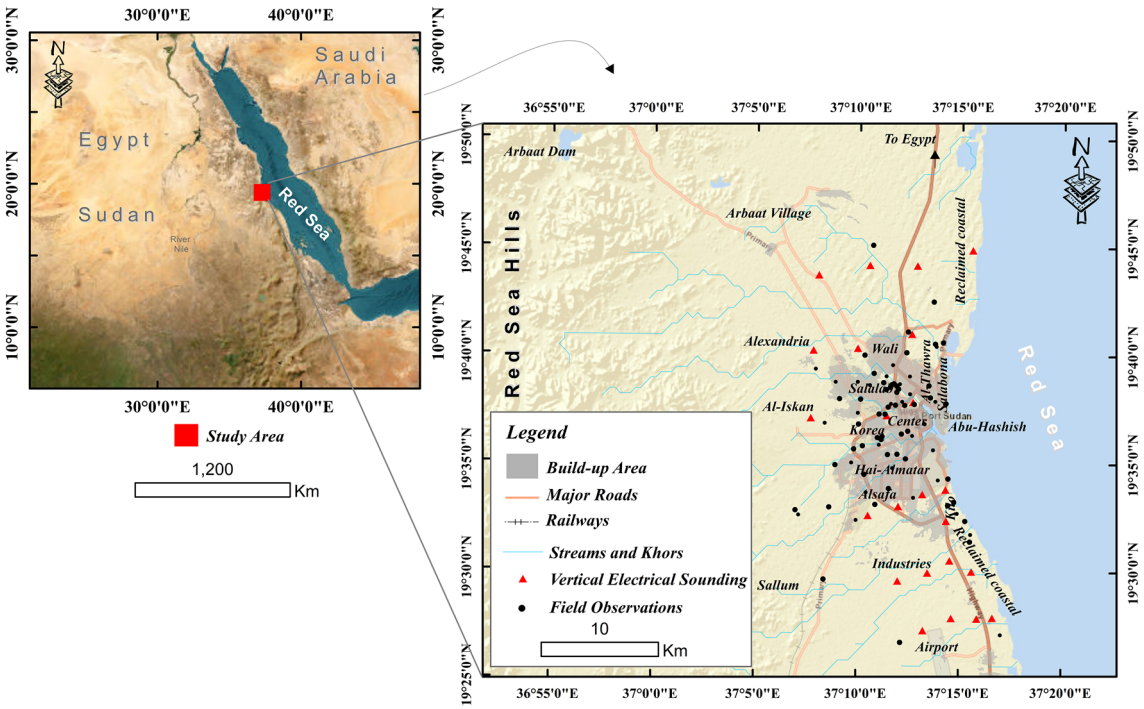

Fig. 1 Regional location of the study area showing Port Sudan along the western Red Sea coast, major physiographic and hydrogeological features. Black dots indicate detailed urban districts, highlighting major neighborhoods and peri-urban districts. Red dots represent vertical electrical sounding (VES) measurements

sabkha deposits. These materials have high porosity and capillarity, which promote moisture retention and salt accumulation (Al-Imam et al. 2015; Daoud et al. 2025). Engineering and geophysical studies show that the (0–20 m) of the subsurface are dominated by unconsolidated silty sands, fine sands, and marine or alluvial sediments, underlain by fractured and weathered coral reef limestone (Kheiralla and Al-Imam 2013). High evaporation, shallow saline groundwater, and capillary rise contribute to persistent soil moisture and the formation of salt crusts.

Hydrogeologically, Port Sudan is underlain by a shallow coastal aquifer strongly influenced by marine intrusion, with groundwater levels commonly rising to within 0–5 m above mean sea level in coastal and sabkha areas (Elsheikh and Elsayed 2015; Siddig et al. 2025) However, elevated salinity and electrical conductivity (EC) in Port Sudan cannot be attributed solely to total dissolved solids (TDS) or direct seawater influence. In addition to marine intrusion extending approximately 6–8 km inland, salinity patterns are intensified by soil–water ionic interactions within evaporite-rich sabkha and coastal plain sediments. These deposits contain abundant soluble salts (e.g., Na^+, Cl^-, SO_4^{2-}), as well as exchangeable clay-bound ions that can elevate TDS values (often exceeding 5000 mg/L near the shoreline) without necessarily reflecting direct seawater salinity (Abdelbagi and Mohamed 2024; Taha et al. 2015). In this setting, a distinct freshwater–seawater interface is absent; instead, a broad mixing zone exists, controlled by shallow groundwater levels, tidal forcing, episodic freshwater inflows from wadis, and strong evaporative concentration.

The combination of climatic, geological, and hydrogeological factors makes the area highly susceptible to hydro-saline degradation. Shallow saline groundwater, high evaporation, and limited vegetation result in persistent surface moisture, salt-crust formation, and a gradual loss of soil strength.

3 Materials and Methods

This study uses remote sensing technology alongside land-use analysis, field calibration, and statistical modeling to examine hydro-saline dynamics driven by urban growth in Port Sudan, a similar approach to those recognized as effective for mapping land-use changes in Sudan (Hasoba et al. 2025; Hawash et al. 2021). Satellite imagery was processed to derive salinity and moisture indicators, which were validated against ground-based electrical resistivity measurements (Dey et al. 2025). Operational thresholds were then defined and applied to map hydro-saline affected areas, followed by correlation analysis and time-series forecasting to evaluate future trends as shown in Fig. 2.

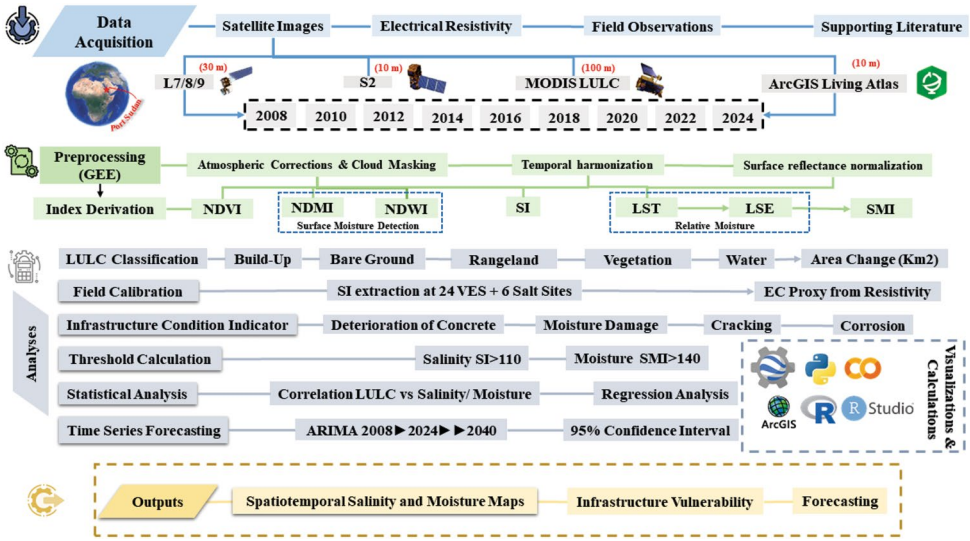

Fig. 2 Conceptual workflow illustrating data sources, processing steps, and analytical methods used in this study, including multi-temporal satellite datasets, field calibration, statistical analysis, and predictive modeling

Table 1 Remote sensing and supplementary datasets used in the present study

Data Source	Sensor / Product	Spatial Resolution	Temporal Coverage	Bands Used	Purpose in Study	Access Platform
Landsat-7 ETM+	Collection 2 Tier 1 Surface Reflectance	30 m (optical), 60 m (thermal)	2008–2012	Blue, Green, Red, NIR, SWIR1, SWIR2, TIR	NDVI, NDMI, SI, LST, LSE, SMI	Google Earth Engine / USGS
Landsat-8/9 OLI/TIRS	Collection 2 Tier 1 Surface Reflectance	30 m (optical), 100 m (thermal)	2014–2024			
Sentinel-2 MSI	Harmonized Surface Reflectance	10–20 m	2016–2024	Blue, Green, Red, NIR, SWIR		
MODIS	MCD12Q1 Land Cover	250 m	2008–2014	LULC classes	Long-term LULC trends	NASA
ArcGIS Living Atlas	ESA World Cover / Dynamic World	10 m	2020–2024		High-resolution LULC mapping	ArcGIS Online
Field data	VES (Electrical Resistivity)	Point-based Wenner array method	Field check	Apparent resistivity → EC	Salinity calibration & validation	Field survey
	Solar salt sites	Point-based GPS		Visual salt crust	Threshold validation	

3.1 Remote Sensing Data Acquisition and Preprocessing

Multi-temporal Landsat-7 ETM+, Landsat-8/9 OLI/TIRS (L7/8/9), and Sentinel-2 MSI (S2) surface-reflectance imagery were analyzed for nine representative years between 2008 and 2024. Data were processed using Google Earth Engine (GEE) (www.earthengine.google.com), ensuring consistent atmospheric correction and cloud masking (<1% cloud cover). Spatial outputs and cartographic layouts were finalized in ArcGIS 10.5. Detailed sensor specifications and product information are summarized in Table 1. To ensure that the observed changes in salinity and moisture reflect long-term trends rather than short-term seasonal variability, all satellite images used for salinity and moisture analysis were acquired during the same climatological window in each observation year. Specifically, L7/8/9 and S2 scenes were selected exclusively from the dry season (between early May and late July) for all analyzed years (e.g., 1 May–31 July 2008; same window applied for subsequent years). No wet-season or post-rainfall imagery was included. Similarly, LULC data were treated differently, as they represent cumulative annual change; therefore, full-year datasets (January–December) were used to characterize land transformation.

3.2 Salinity and Moisture Indices

3.2.1 Rationale and Formulation

Soil salinity was evaluated using a SWIR-based Salinity Index (SI) (Eq. 1), selected over alternative formulations (e.g., SI-1, SI-2) due to its enhanced sensitivity to the diagnostic spectral responses of halite and evaporitic crusts. This index was originally developed and validated under arid coastal conditions comparable to those of Port Sudan City, particularly in environments analogous to those of Saudi Arabia (Elhag 2016). Preliminary tests showed that this

index minimized background noise from highly reflective, sandy desert soils better than traditional square-root combinations of near-infrared (NIR) and Red, and it was more sensitive to saline surfaces commonly found in sabkha and reclaimed coastal terrains (Abuelgasim and Ammad 2019).

$$SI = SWIR_1 \,.\, \mathrm{Red}/Blue \tag{1}$$

Soil moisture conditions were characterized using the Normalized Difference Moisture Index (NDMI), which exploits the strong water absorption feature in the SWIR region and is effective over sparsely vegetated and bare soils typical of arid coastal environments (Metternicht and Zinck 2003). NDMI was computed consistently for both L7/8/9 and S2 imagery using spectrally comparable NIR and SWIR bands to enable cross-sensor comparison and temporal continuity (Eq. 2) (Liuzzo et al. 2020). This harmonized formulation minimizes sensor-specific radiometric differences and allows moisture patterns derived from different platforms to be directly compared across the 2008–2024 time series. The combined use of L7/8/9 and S2 therefore provides long-term temporal coverage together with improved spatial detail, strengthening the detection of moisture dynamics associated with urban expansion. In addition, the Normalized Difference Water Index (NDWI) was derived from S2 imagery to delineate and mask open water bodies and persistently inundated surfaces (Eq. 3), ensuring that NDMI-based moisture signals reflect soil and near-surface moisture rather than standing water (Bai et al. 2019; Sharma et al. 2022; E. Wang et al. 2025; J. Wang et al. 2021).

$$NDMI = \frac{NIR - SWIR}{NIR + SWIR} \tag{2}$$

where *NIR* is the reflectance in the near-infrared band, and Red is the reflectance in the red band.

$$NDWI = \frac{Green - NIR}{Green + NIR} \tag{3}$$

Land Surface Temperature (LST) (Eq. 4) and Land Surface Emissivity (LSE) – referred to as (ε) in Eq. (6) were derived following the Normalized Different Vegetation Index (NDVI)-based emissivity approach (Avdan and Jovanovska 2016; Niclòs et al. 2021; Vanhellemont 2020). Fractional vegetation cover (PV) was computed from NDVI (Eqs. 7–8) and used to estimate emissivity. The Soil Moisture Index (SMI) was computed by normalizing LST values representing relative surface moisture variability (Appendix A: Table 6). The LST calculated following different steps as shown in Eqs. 4–9:

$$LST = \frac{BT}{1 + \left(\frac{\lambda BT}{C_2}\right) ln\,(\varepsilon)} \tag{4}$$

BT is top of Atmosphere brightness temperature; λ is the effective wavelength of the thermal band (μm) (L9 Band10 λ = 10.8 and Band11 λ = 12); ε is land surface emissivity (LSE); and C_2 is the second radiation constant (μm·K):

$$C_2 = \frac{(h * c)}{k} \tag{5}$$

where h is Planck's constant (6.626×10^{-34} J·s), c is the speed of light in vacuum (2.998×10^{8} m·s^{-1}), and k is the Boltzmann constant (1.38×10^{-23} J·K^{-1}). Accordingly, the second radiation constant C_2 is equal to 14,388 μm·K.

$$\varepsilon = 0.004PV + 0.986 \tag{6}$$

PV represents the proportion of vegetation cover derived from NDVI.

$$PV = (NDVI - NDVI_{\min}/NDVI_{\max} - NDVI_{\min})^2 \tag{7}$$

where $NDVI_{min}$ and $NDVI_{max}$ denote the minimum and maximum NDVI values observed within the image, respectively.

$$NDVI = \frac{NIR - Red}{NIR + Red} \tag{8}$$

where Red and NIR are the red and near-infrared reflectance bands.

$$SMI = (LST_{\max} - LST)/(LST_{\max} - LST_{\min}) \tag{9}$$

where: LST_{max} and LST_{min} are the scene-specific dry and wet bounds (per acquisition date), and SMI is unitless, representing relative surface moisture conditions.

3.2.2 Shallow Direct Current Electrical Resistivity Measurements

Shallow subsurface electrical resistivity measurements were conducted using a SAS1000 Terrameter (ABEM Instrument AB) with a Schlumberger electrode configuration, where the current electrodes (A–B) are progressively expanded while the potential electrodes (M–N) remain near the array center (Dahlin and Zhou 2006; Telford et al. 1990). The survey employed a current electrode spacing of AB = 3.0 m and a potential electrode spacing of MN = 1.0 m. In the Schlumberger array, the depth of investigation is mainly controlled by the current-electrode separation, yielding an effective

penetration depth of approximately 0.3–0.9 m, appropriate for near-surface salinity and moisture characterization (Loke 2004). Apparent resistivity values were calculated internally from measurements of injected current resulting potential difference ΔV and I. Electrical resistance R was computed as (Eq. 10):

$$R = \frac{\Delta V}{I} \tag{10}$$

The apparent resistivity (ρ_a) was then obtained using the Schlumberger geometric factor (K) (Eq. 11):

$$\rho_a = K \times R \tag{11}$$

where the geometric factor was defined as (Eq. 12):

$$K = \pi \left(\frac{(AB/2)^2 - (MN/2)^2}{MN} \right) \tag{12}$$

Under favorable electrode contact conditions, the uncertainty associated with apparent resistivity measurements is typically within ± 2–5%, which is acceptable for shallow environmental and hydro-salinity investigations and does not affect the relative interpretation of resistivity patterns (Dwamena and Mensah 2026; Telford et al. 1990).

3.2.3 Threshold Determination for Salinity and Moisture

Given the near-zero vegetation cover of the study area (see Table 2), the indices primarily reflect the spectral response of surface salt crusts, sabkha soils, and moisture-rich sediments rather than vegetation effects, enhancing their suitability for hydro-saline detection in this arid coastal environment. Operational thresholds separating saline from non-saline surfaces were established using a combined field-calibrated and statistically informed approach. Satellite-derived SI values were compared with electrical conductivity (EC, dS m^{-1}) measurements collected at 24 representative ground locations, including Vertical Electrical Sounding (VES) measurements and active solar salt production sites distributed across coastal, reclaimed, and inland zones (see Fig. 1). SI values ranged from 1.01 to 1.80, corresponding to EC values between 0.13 and 20 dS m^{-1} (Appendix A: Tables 7 and 8). Linear regression analysis (Appendix A: Figs. 20 and 21) yielded the following calibration relationship (Eq. 13):

$$EC = 29.242 \times \mathrm{SI} - 27.448 (R^2 = 0.716) \tag{13}$$

Based on field verification conducted at 24 representative locations in urban and peri-urban districts of Port Sudan,

Table 2 Spatiotemporal variability of LULC classes and soil salinity and moisture conditions between 2008 and 2024, reported as percentages (%) and equivalent areas (km^2)

Year	Salinity		Moisture		Built-Area		Bare-ground		Rangeland		Crops		Water	
	%	km^2	%	km^2	%	km^2	%	km^2	%	km^2	%	km^2	%	km^2
2008	4.02	8.12	8.48	120.15	8.71	65.87	80.42	608.81	10.86	82.06	0.01	0.01	254.98	254.98
2010	5.57	11.24	9.54	135.12	9.37	70.93	78.70	595.96	11.89	90.05	0.04	0.04	254.57	254.57
2012	8.40	16.97	10.20	144.50	9.37	71.33	77.25	588.17	13.32	101.38	0.07	0.07	254.88	254.88
2014	10.16	20.51	10.65	150.84	10.19	77.20	71.00	538.39	18.80	112.62	0.01	0.01	254.78	254.78
2016	12.90	26.04	11.23	159.17	11.10	80.95	66.34	483.04	22.52	163.71	0.04	0.04	254.88	254.88
2018	12.18	24.60	11.55	163.67	11.14	83.17	57.72	430.93	31.07	242.33	0.07	0.07	255.48	255.48
2020	13.46	27.18	10.15	143.86	13.93	105.84	40.51	307.80	45.40	342.10	0.16	0.16	254.98	254.98
2022	13.33	26.92	10.91	154.54	14.32	108.06	38.15	287.26	47.45	361.32	0.08	0.08	254.88	254.88
2024	19.99	40.36	17.32	245.49	16.89	131.13	28.48	221.29	54.34	422.43	0.29	0.29	255.18	255.18

including Salalab, Al-Thawra, Walli, Salabona, Korea, Dem Mayo, and Iskan (see Appendix A: Fig. 22), where salinity-related deterioration such as concrete scaling, salt efflorescence, reinforcement corrosion, and foundation damage was consistently observed, a salinity threshold of SI = 1.10 was selected. According to the empirical calibration (Eq. 13), this index value corresponds to an electrical conductivity of approximately EC = 4.7 dS m^{-1}, a level widely recognized as aggressive to construction materials under arid coastal sabkha conditions (Akça et al. 2020; Peters et al. 2025; Salem and Jia 2024). For raster classification, this threshold corresponds to a grayscale digital number of DN = 110 in an 8-bit (0–255) representation, and pixels exceeding this value were classified as saline. A corresponding moisture threshold was defined using the SMI. Guided by field observations of persistently damp ground surfaces, shallow capillary soil moisture zones, and moisture-induced material degradation (e.g., plaster peeling and foundation dampness), a grayscale threshold of DN = 140 was adopted to delineate high-moisture conditions. Pixels exceeding this value represent areas of elevated near-surface moisture, rather than open or standing water. Both thresholds represent relative intensity levels rather than absolute physical boundaries. The SI is derived from multispectral reflectance and captures the surface expression of salt accumulation, while the SMI is obtained through thermal normalization of land surface temperature, whereby LST values are scaled between scene-specific dry (maximum LST) and wet (minimum LST) surface bounds to express relative moisture conditions. This normalization highlights spatial contrasts in surface wetness while minimizing sensor- and scene-dependent thermal variability. Consequently, the indices emphasize spatial patterns and temporal changes, rather than direct laboratory-equivalent measurements of electrical conductivity or volumetric water content.

To minimize uncertainty associated with transient wet conditions, defined here as short-duration surface wetness persisting from hours to several days following rainfall or temporary ponding, only cloud-free satellite scenes acquired during the complete dry season were used. No wet-season imagery was included in the analysis. As a result, the detected salinity and moisture patterns reflect chronic, structurally relevant hydro-saline conditions controlled by shallow groundwater, capillary rise, and soil properties, rather than episodic rainfall responses. This thresholding strategy follows established practices in arid-region remote sensing, where selective yet representative ground validation is used to define operational salinity and moisture limits relevant to environmental and infrastructure risk assessment (Bannari et al. 2018; Boutin et al. 2023; Gao et al. 2025).

3.3 Land Cover Classification

LULC dynamics were quantified using MODIS land-cover products for consistent long-term trend analysis (2008 to 2018) (Cover and Change 1999), and ArcGIS Living Atlas datasets (ESA WorldCover and Dynamic World) (2020–2024) for high-resolution spatial mapping. Built-up, bare ground, rangeland, vegetation and water classes were extracted and summarized as area statistics (km^2) for each year.

3.4 Field Survey and Calibration

Systematic field observations of surface and structural conditions were recorded across the study area. Areas with high SI and EC consistently exhibited surface salt crusts, damp soil patches, and darkened moisture bands, indicating persistent capillary rise and influence from shallow saline groundwater. In built-up and reclaimed zones, these hydro-saline conditions were associated with progressive deterioration of construction materials. At the structural scale, irregular cracking, differential settlement, and foundation distress were frequently observed in buildings constructed on untreated saline soils.

Ground-based validation was conducted to support the calibration and interpretation of satellite-derived salinity and moisture indices and to verify their relevance to infrastructure deterioration processes. Field surveys comprised 24 VES profiles distributed across representative coastal sabkha zones, reclaimed urban areas, and inland background soils, together with six active solar salt production sites characterized by visible salt efflorescence (see Fig. 1 and Appendix A: Fig. 22).

3.5 Statistical and Predictive Analysis

Pearson's correlation and linear regression were applied to quantify relationships between LULC classes (built-up, rangeland, bare ground) and salinity- or moisture-affected areas. Future trajectories to 2040 were explored using ARIMA time-series forecasting with model selection based on AIC minimization and residual diagnostics (Hyndman et al. 2025). Forecast uncertainty was reported using 95% prediction intervals, and projections are interpreted as potential trends rather than deterministic outcomes, given the limited number of observation years. All datasets were analyzed and visualized in R (version 4.3) using the "ggplot2" package (R. Core Team 2024).

4 Results

4.1 Multi-Sensor Detection of Salinity and Moisture Dynamics (2008–2024)

To monitor hydro-saline dynamics in Port Sudan, this study utilized a multi-sensor, multi-temporal approach, integrating L7/8/9 and S2 satellite datasets. This integration optimizes the trade-off between temporal depth and spatial granularity. Specifically, the extensive Landsat archive enables the observation of decadal-scale shifts (30m), while the superior resolution of Sentinel enables the characterization of fine-scale urban patterns (10m). This dual-scale analysis ensures a more robust interpretation of environmental dynamics, particularly within complex, densely built environments where Landsat's coarser resolution may be insufficient.

Elevated salinity was largely restricted to coastal sabkha and tidally influenced depressions in 2008 (see black box and arrows in Fig. 3a). Saline surfaces extended beyond the immediate coastal areas, with clear inland expansion toward the southern part of the study area by 2012 (Fig. 3b). A comparable shift is observed in soil moisture patterns: in 2008, higher moisture values were concentrated in nearshore lowlands (Fig. 3c), whereas by 2012, moisture extended inland toward urbanized southern districts (Fig. 3d). This early inland migration indicates increasing surface-water retention and declining drainage efficiency associated with expanding urban land use.

To ensure objective classification of saline and moist surfaces, operational thresholds were defined using a combined remote-sensing and field-calibrated approach. High salinity and moisture classes were identified using SI > 110 and SMI > 140, respectively (see Eq. 13). The salinity threshold (SI = 110) corresponds to approximately 43% of the cumulative SI distribution and marks the transition at which field-verified saline conditions consistently occur (see Figs. 13 and 14). Because SI and SMI are unitless, index-based measures derived from spectral and thermal responses, they represent relative intensity rather than absolute EC or volumetric moisture; nevertheless, they provide spatially consistent detection of hydro-saline hotspots and temporal change patterns across the study area (see Appendix B).

L7/8/9-derived salinity maps reveal a progressive inland migration of salinity from 2014 to 2024 (Fig. 4a–f). Saline surfaces increasingly encroach into reclaimed lands, drainage corridors, and urban districts, including Salalab, Walli, Alexandria, Abu-Hashish, Al-Iskan, Alsafa, Hai Al-Matar, industrial zones, the Airport district, and Sallum (see Fig. 1 and Appendix A: Fig. 22). S2 salinity maps further resolve fine-scale urban features and consistently identify elevated salinity in narrow open spaces adjacent to roads and building blocks (see Fig. 5a–f). These zones act as salt-accumulation strips, where capillary rise and poor infiltration concentrate dissolved salts. In contrast, roads and rooftops often appear less saline in surface reflectance because impermeable construction materials mask subsurface conditions (see Fig. 18 and Appendix A: Fig. 22). This distinction is critical for interpretation: while remote sensing captures surface expressions of salinity, field evidence confirms that subsurface salinity beneath built-up areas continues to drive infrastructure deterioration even where surface signals are muted.

Soil moisture patterns derived from L7/8/9 NDMI/SMI (Fig. 6a–f) show interannual variability but a clear long-term increase in low-lying drainage systems, flood-prone corridors, reclaimed coastal zones, and urban rangelands. S2 soil moisture maps highlight localized moisture accumulation along infrastructure boundaries and frequently overlap with saline zones, consistent with shallow groundwater influence, surface water stagnation, and inefficient urban drainage (Fig. 7a–f).

The high-resolution comparison of 2014 and 2024 conditions summarizes the decadal transformation (Figs. 8 and 9). In 2014, high salinity (SI > 110) was primarily confined to coastal sabkhas and poorly drained depressions (Fig. 8a), whereas by 2024, salinized areas expanded substantially inland, with extensive zones exceeding SI > 130, indicative of intensified salt-crust development (Fig. 8b). Moisture exhibits a parallel trend: in 2014, high moisture (SMI > 140) was largely limited to natural drainage basins (Fig. 9a), while by 2024, high-moisture zones expanded into newly urbanized and peri-urban spaces, with widespread patches exceeding SMI > 160 (Fig. 9b). Importantly, many areas of elevated moisture coincide spatially with high salinity, indicating compounded hydro-saline stress conditions that are particularly detrimental to building foundations and near-surface construction materials.

A key urban-scale pattern revealed by S2 is the systematic concentration of salinity within transitional strips between buildings and adjacent paved roads (Figs. 8b, 9b; see also Fig. 18). These strips function as accumulation zones where runoff is trapped by impermeable surfaces and salts concentrate through capillary-driven processes. Conversely, building footprints themselves may exhibit lower surface SI values because construction materials (e.g., concrete, asphalt, and roofing) mask the spectral reflectance of the underlying soil in optical satellite imagery, thereby reducing the surface expression of salinity. This reflects a known limitation of surface-based salinity detection in dense urban environments, where subsurface salinity and moisture may persist and actively contribute to material deterioration despite weak or absent surface spectral responses. Field observations of corrosion, foundation cracking, and material deterioration in these settings therefore underscore

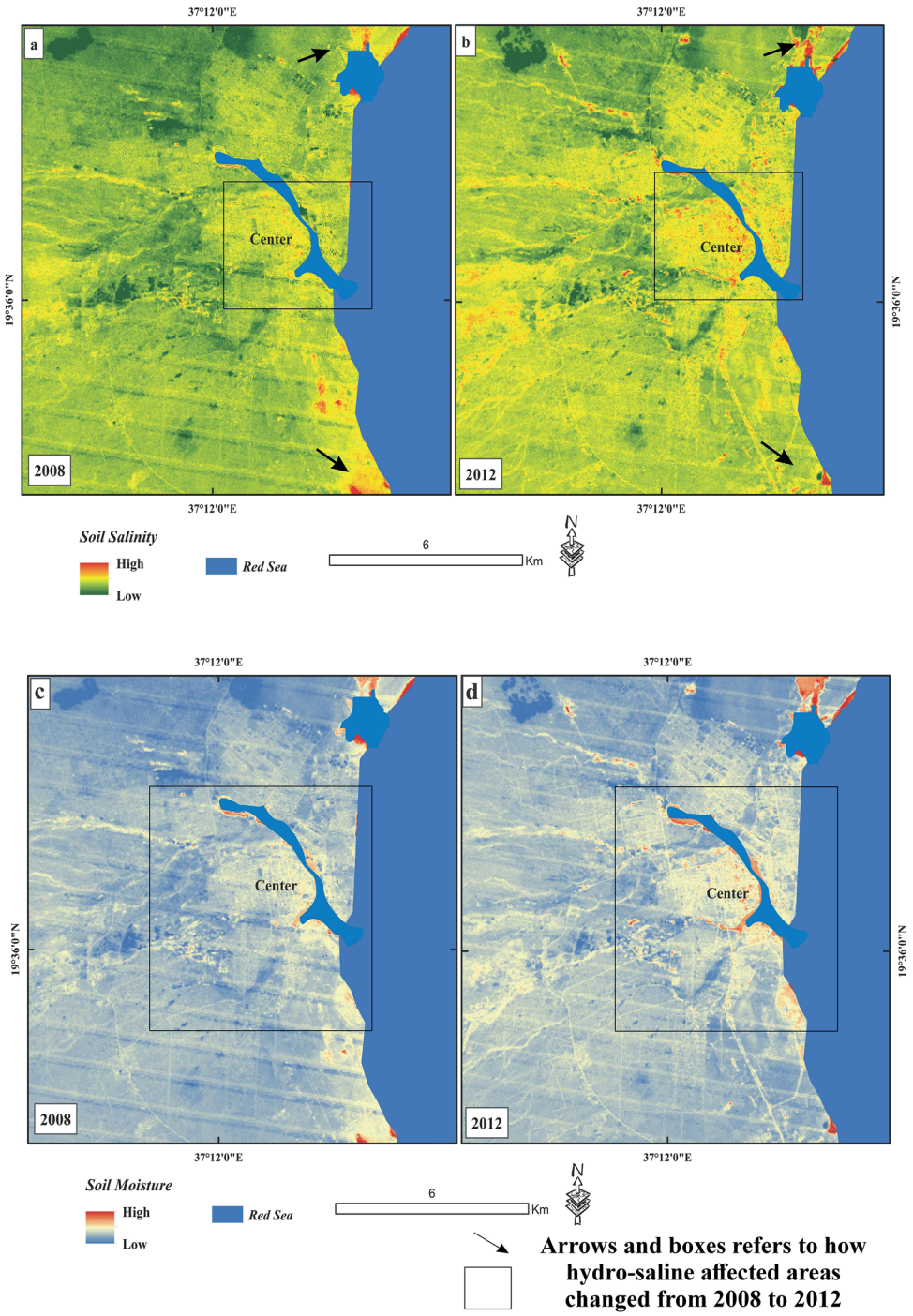

Fig. 3 Early-period Landsat-based hydro-saline conditions in Port Sudan showing (**a**–**b**) soil salinity for 2008 and 2012 and (**c**–**d**) soil moisture for 2008 and 2012, respectively. Maps are displayed using consistent relative index scales within each variable to illustrate early inland expansion trends

the importance of interpreting SI and SMI maps alongside ground evidence, particularly in highly built-up districts.

Multi-year salinity and moisture maps reveal a coherent and progressive trajectory of hydro-saline expansion across Port Sudan. Salinity shows a clear inland migration pattern, evolving from its initial confinement within coastal sabkha environments in the early years (Fig. 3a) toward low-lying inland and reclaimed zones by 2024 (Fig. 8b). This expansion follows elongated pathways aligned with natural drainage lines and topographic depressions, becoming more pronounced after 2016 and spatially continuous in the later period. Soil moisture exhibits a broadly similar, but more temporally dynamic, pattern. In the early years, moisture anomalies were sparse and largely restricted to coastal lowlands (Fig. 3c). In subsequent periods, persistent moisture retention emerged in urban corridors, reclaimed lands, and expanding rangelands, particularly in low-elevation sectors with shallow groundwater and impaired drainage (Fig. 9b).

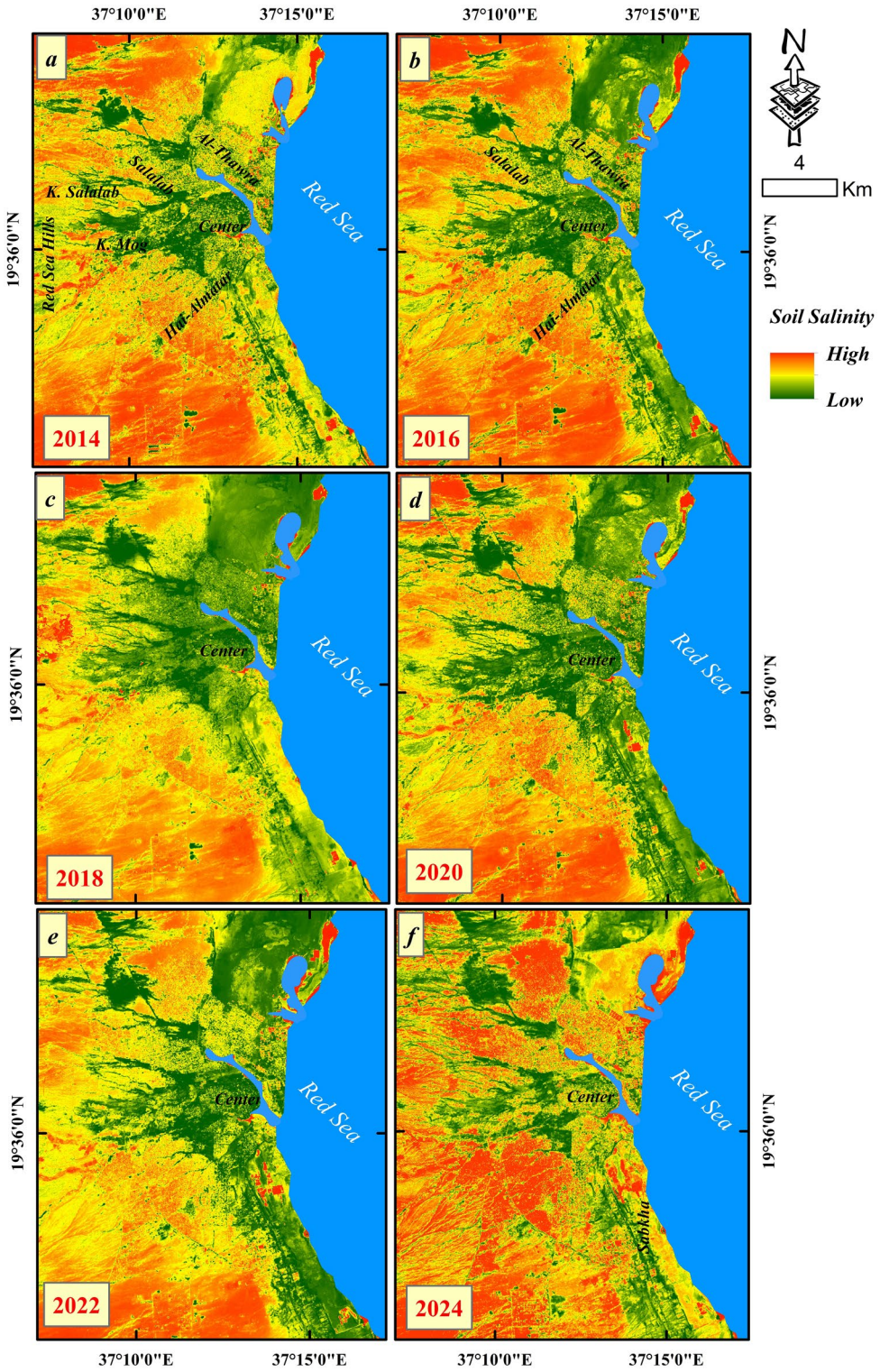

Fig. 4 Multi-temporal soil salinity distribution in Port Sudan derived from L8/9 salinity indices for (**a**) 2014, (**b**) 2016, (**c**) 2018, (**d**) 2020, (**e**) 2022, and (**f**) 2024. All maps are plotted using a fixed color scale to allow direct temporal comparison

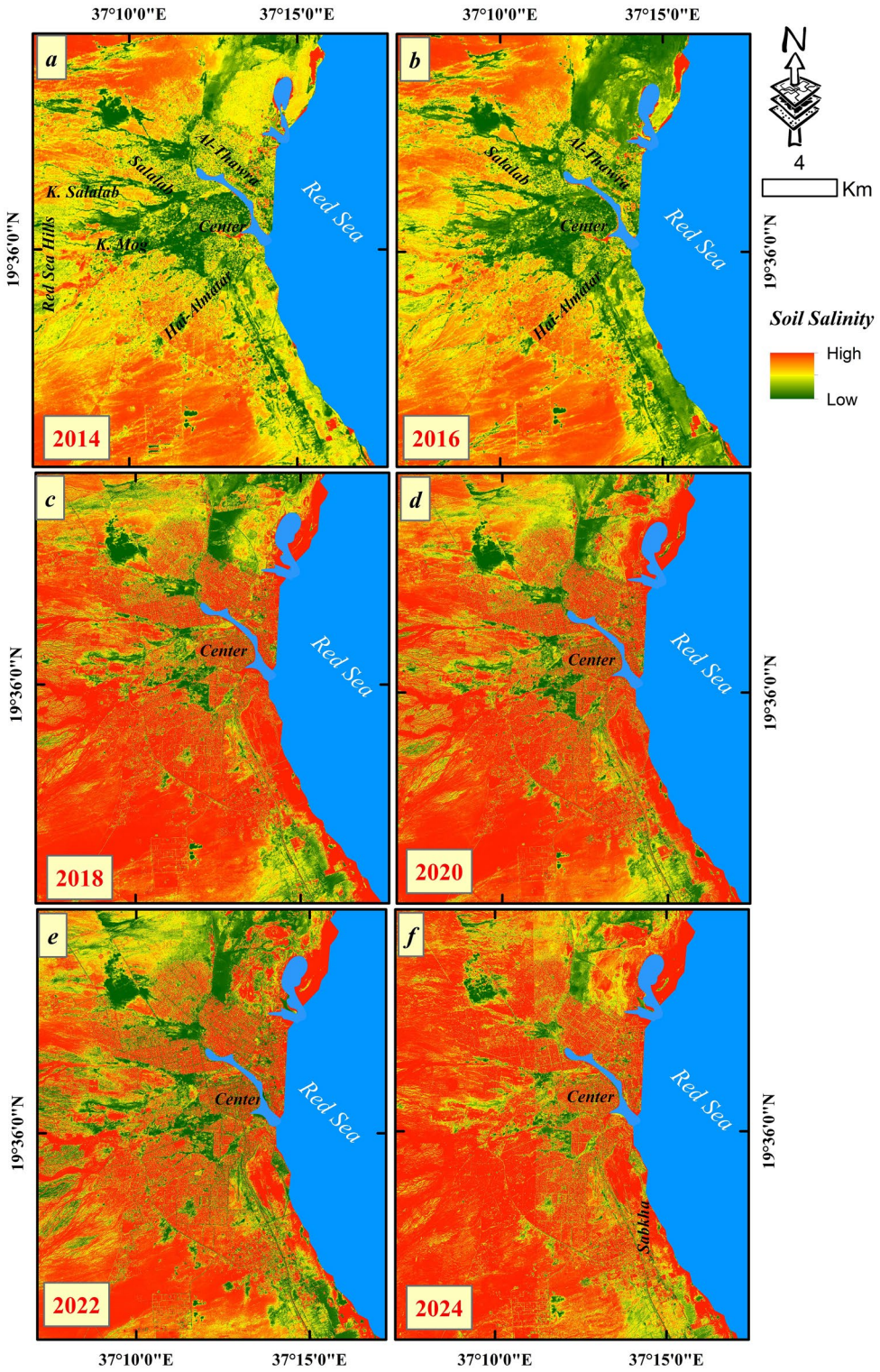

Fig. 5 Multi-temporal soil salinity distribution in Port Sudan derived from S2 salinity indices for years (**a**) 2014, (**b**) 2016, (**c**) 2018, (**d**) 2020, (**e**) 2022, and (**f**) 2024

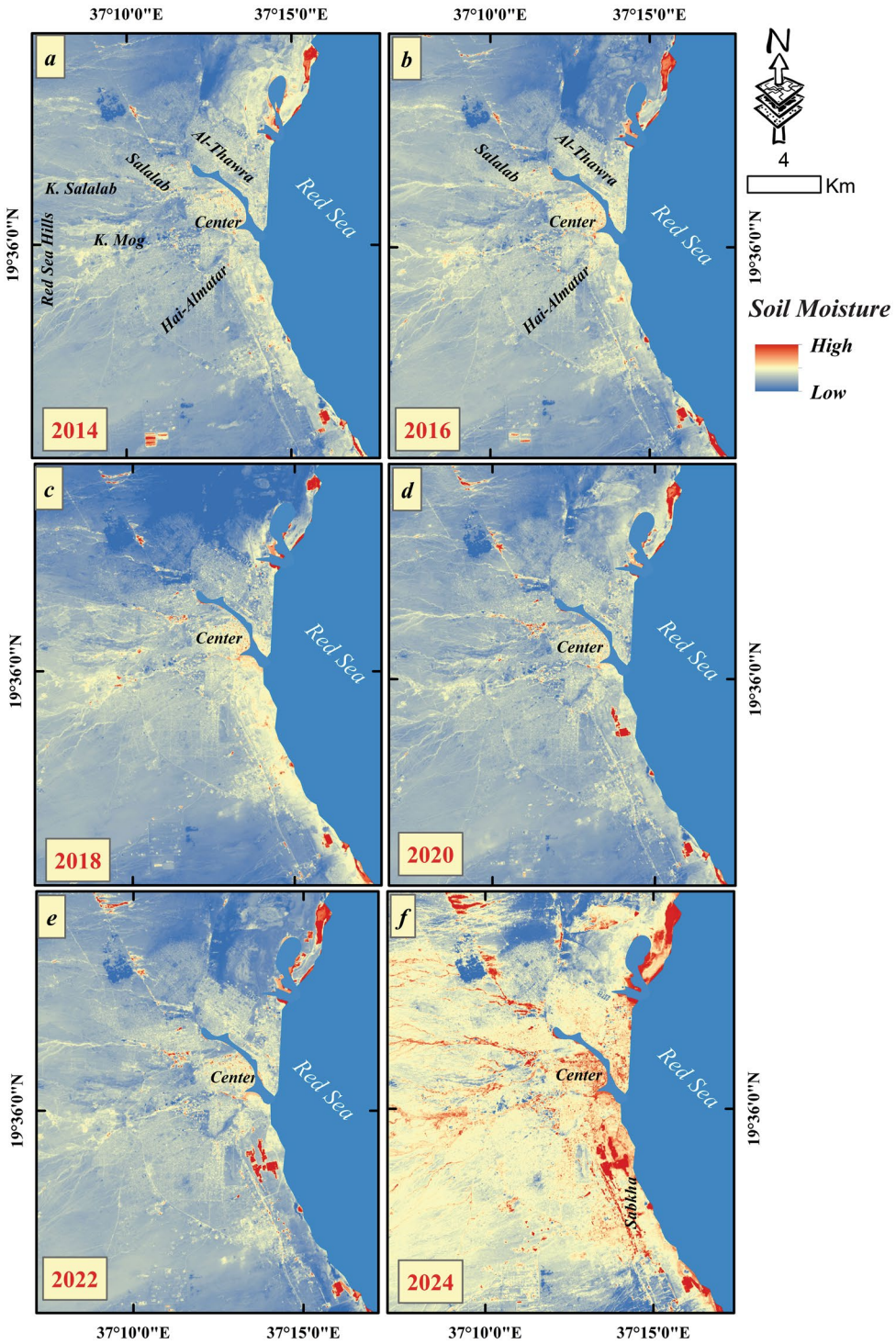

Fig. 6 Multi-temporal soil moisture distribution in Port Sudan derived from Landsat SMI for (**a**–**f**) 2014–2024. Maps use a consistent relative moisture scale to illustrate progressive expansion of moisture-retention zones, including years influenced by anomalous rainfall events

A key spatial characteristic is the frequent co-occurrence of high salinity and high moisture in reclaimed and low-lying urban zones. This overlap indicates coupled hydro-saline processes, whereby sustained moisture availability enhances salt mobilization, capillary rise, and surface accumulation. In contrast, elevated and undeveloped inland areas display weaker and less persistent hydro-saline signatures, reflecting better natural drainage and lower groundwater influence.

4.2 LULC Change Detection (2008–2024)

LULC maps for Port Sudan (Fig. 10a–f) classify the landscape into built-up areas, bare soil, rangeland, and vegetation

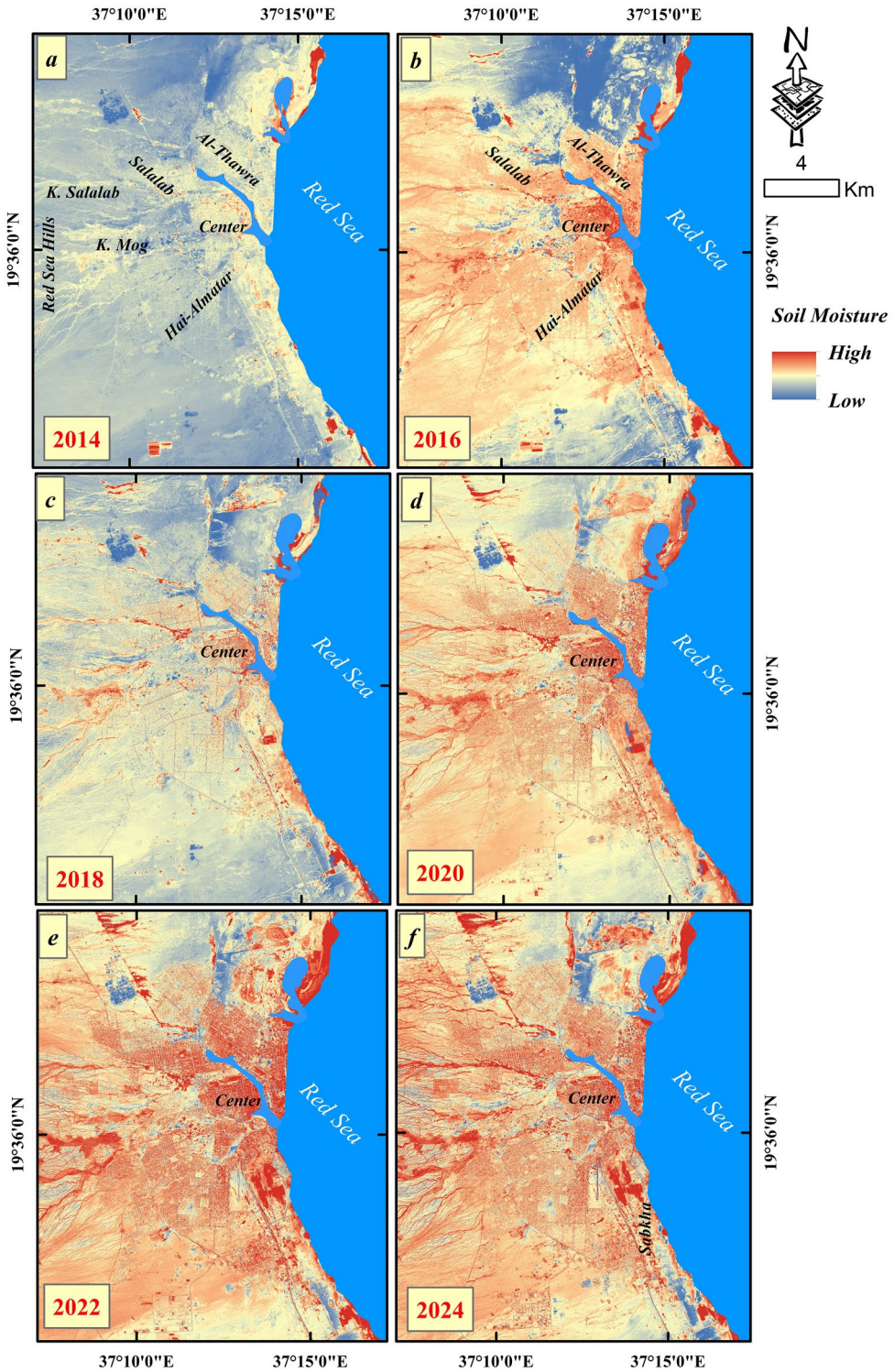

Fig. 7 Sentinel-2 NDMI–derived soil moisture distribution for the same years as Fig. 6, showing enhanced spatial detail within urban and reclaimed areas

(trees/crops), excluding water bodies, which exhibit negligible temporal change. The sequence of maps reveals a clear transition from a landscape dominated by bare soil to an increasingly fragmented mosaic characterized by expanding built-up and rangeland classes. Bare soil dominated most of the study area, while built-up land was largely confined to the historic urban core in 2014, including the City Center, Salalab, Falamingo, and Althawra (Fig. 10a; locations shown in Fig. 1). By 2016–2018 (Fig. 10b–c), urban expansion became evident along major transportation corridors and near industrial zones, with progressive conversion of bare soil and marginal rangeland into built-up land,

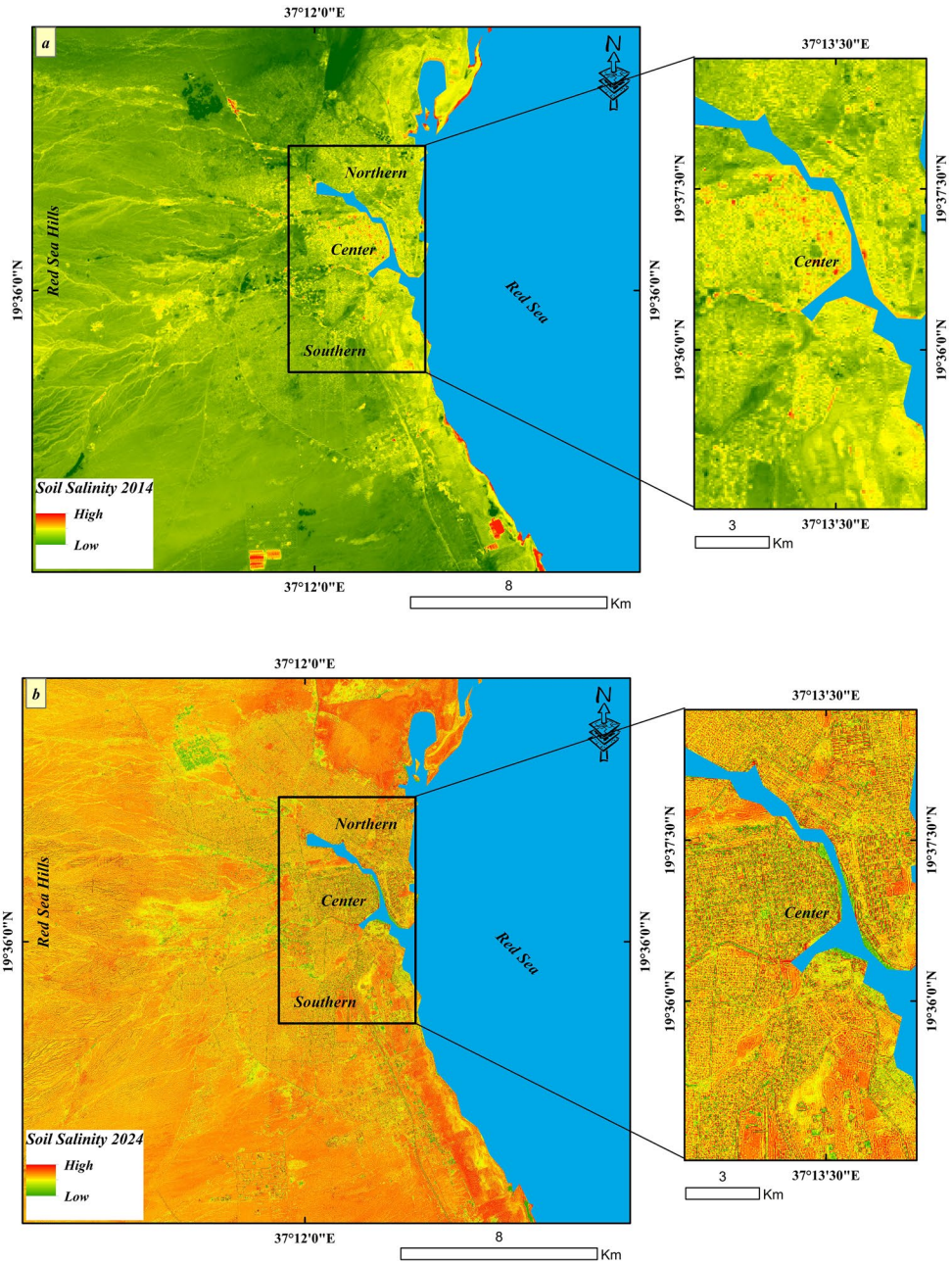

Fig. 8 (**a**) Landsat-derived soil salinity index (SI) map for 2014, showing city-scale salinity distribution dominated by coastal sabkha and low-lying areas; (**b**) Sentinel-2–derived SI map for 2024. The main panel shows city-scale inland expansion of salinity, while the inset illustrates a zoomed urban district where salinity concentrates within transitional strips between buildings and adjacent paved roads. Lower SI values over rooftops reflect spectral masking by construction materials rather than the absence of subsurface salinity

particularly in areas such as Alexandria, the Ring Road, and Filip. From 2020 onward (Fig. 10d–f), urban growth accelerated markedly, extending into eastern and southwestern sectors of the city, including Alsafa, Hai-Almatar, the Airport district, and newly developed industrial areas. Over the same period, rangeland expanded substantially, reflecting both peri-urban growth and land conversion into semi-developed and grazing zones.

Quantitative analysis of LULC changes between 2008 and 2024 confirms this spatial pattern (see Table 2). Built-up areas increased from approximately 6.5% of the study area in 2008 to about 13% in 2024, while bare ground declined sharply from 60.2% to 21.9%. In contrast, rangeland expanded from 8.1% to 41.8%, largely replacing previously undeveloped barren surfaces. Temporal trends in these LULC transitions are further illustrated in the appendix (B and C), which supports the spatial observations derived from the map series. These LULC transformations provide the essential land-surface context for interpreting the concurrent inland expansion of soil salinity and moisture dynamics, particularly within reclaimed, peri-urban areas, and infrastructure-dense zones (Appendix C: Figure C4).

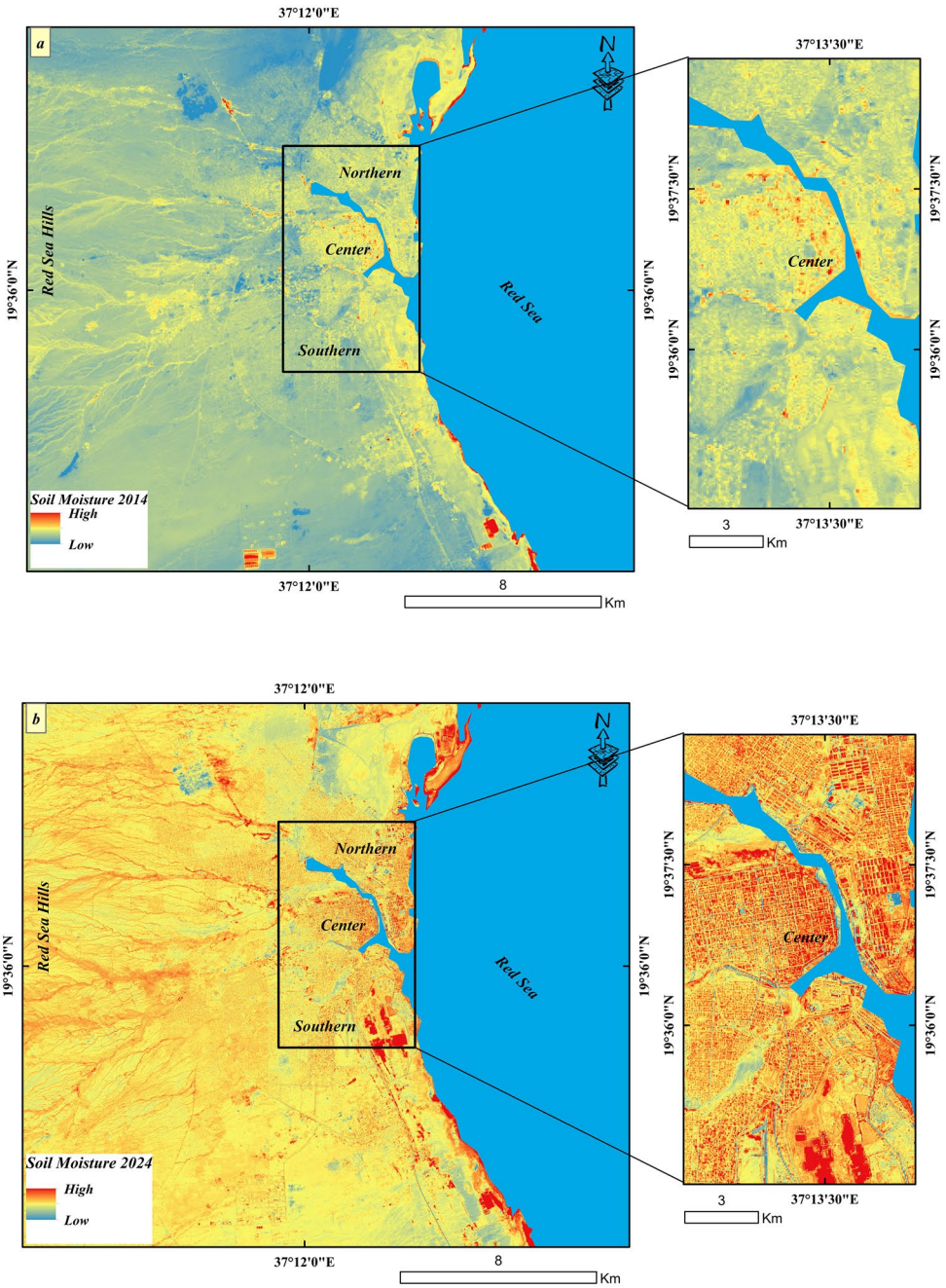

Fig. 9 (**a**) Landsat-derived soil moisture distribution for 2014, highlighting moisture primarily within coastal depressions and drainage pathways; (**b**) Sentinel-2–derived soil moisture distribution for 2024. The city-scale map shows expanded moisture-affected zones, while the inset reveals localized accumulation along infrastructure boundaries and exposed soil margins between buildings and roads. These patterns reflect impaired drainage and shallow groundwater influence in newly urbanized areas

4.3 Urban Expansion as a Driver of Hydro-Saline Intensification

The integrated LULC–salinity–moisture maps for 2014, 2018, and 2024 provide direct spatial evidence that urban expansion is closely associated with hydro-saline intensification (Figs. 11 and 14). Comparative overlays of salinity and moisture patterns with LULC reveal a progressively stronger spatial relationship between land conversion and hydro-saline intensification. In 2014, high-salinity zones were primarily located in coastal sabkha and bare-soil sectors (Fig. 11a–b). By 2018, salinity encroached into bare ground areas undergoing conversion to built-up land and rangeland (Fig. 11c–d). In 2024, salinity reached its maximum inland extent, intersecting extensively with expanding urban and industrial development, especially in reclaimed coastal areas and along transport corridors (Fig. 11e–f). This temporal sequence supports a causal interpretation: expansion into saline-prone terrain, combined with surface modification, increases the exposure of infrastructure and near-surface soils to salinization.

Soil moisture shows similar spatial and temporal patterns (Fig. 12). In 2014, higher moisture was mainly found along

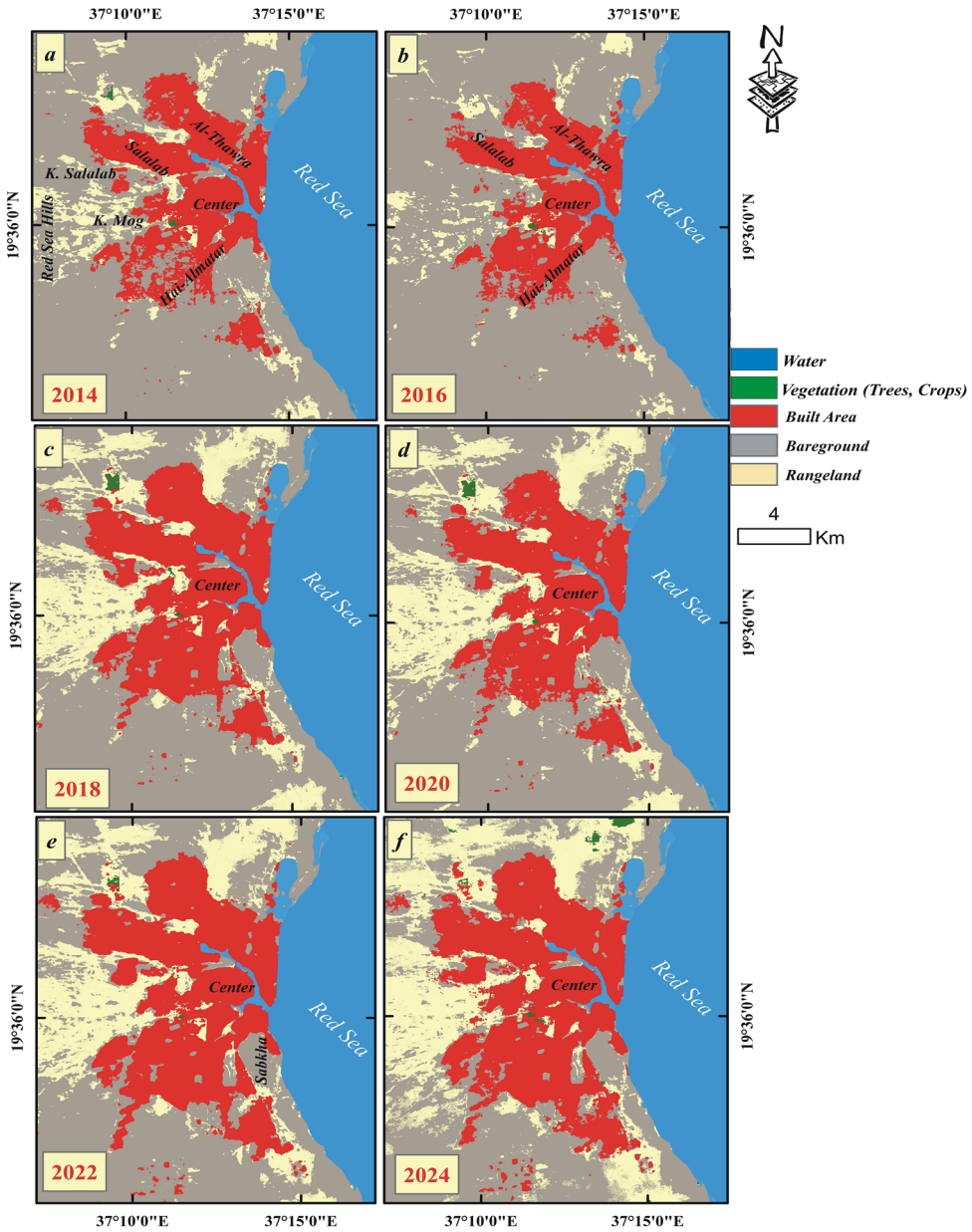

Fig. 10 LULC maps of Port Sudan from (**a**) 2014; (**b**) 2016; (**c**) 2018; (**d**) 2020; (**e**) 2022; to (**f**) 2024 showing progressive expansion of built-up areas and rangeland and corresponding reduction of bare soil, derived from Landsat and ArcGIS Living Atlas datasets

drainage paths and wadis. Built-up areas showed limited surface moisture due to impervious roofs and paved roads, which suppress optical moisture signals and change infiltration routes (Fig. 12a–b). To minimize the effect of short-term extreme rainfall, a different acquisition month was selected for 2018. Even with this change, moisture levels remained high (Fig. 12c–d), especially on bare ground, in reclaimed coastal areas, and in growing residential zones. This persistence indicates that increased moisture is due not only to episodic rainfall but also to long-term hydrological changes, such as rising shallow groundwater, reduced drainage efficiency, and recent climate anomalies characterized by more intense and irregular precipitation. By 2024, high-moisture areas extended further inland and became more common in roads and densely developed regions (Fig. 12e–f), where impermeable surfaces increase runoff and subsurface water retention. Figure 13a–b confirms this trend, showing faster inland movement and intensification of hydro-saline conditions caused by urban growth, drainage disruption, and the combined effects of extreme rainfall and coastal tides. These factors increase waterlogging, promote capillary rise, and worsen hydro-saline vulnerability, directly affecting environmental stability and foundation performance.

An integrated combination of salinity and moisture conditions (Fig. 14) overlays built-up areas (black polygons) with threshold salinity (SI > 110) and moisture (SMI > 140) to consistently identify affected zones over time. Throughout the observation period, elevated salinity and moisture

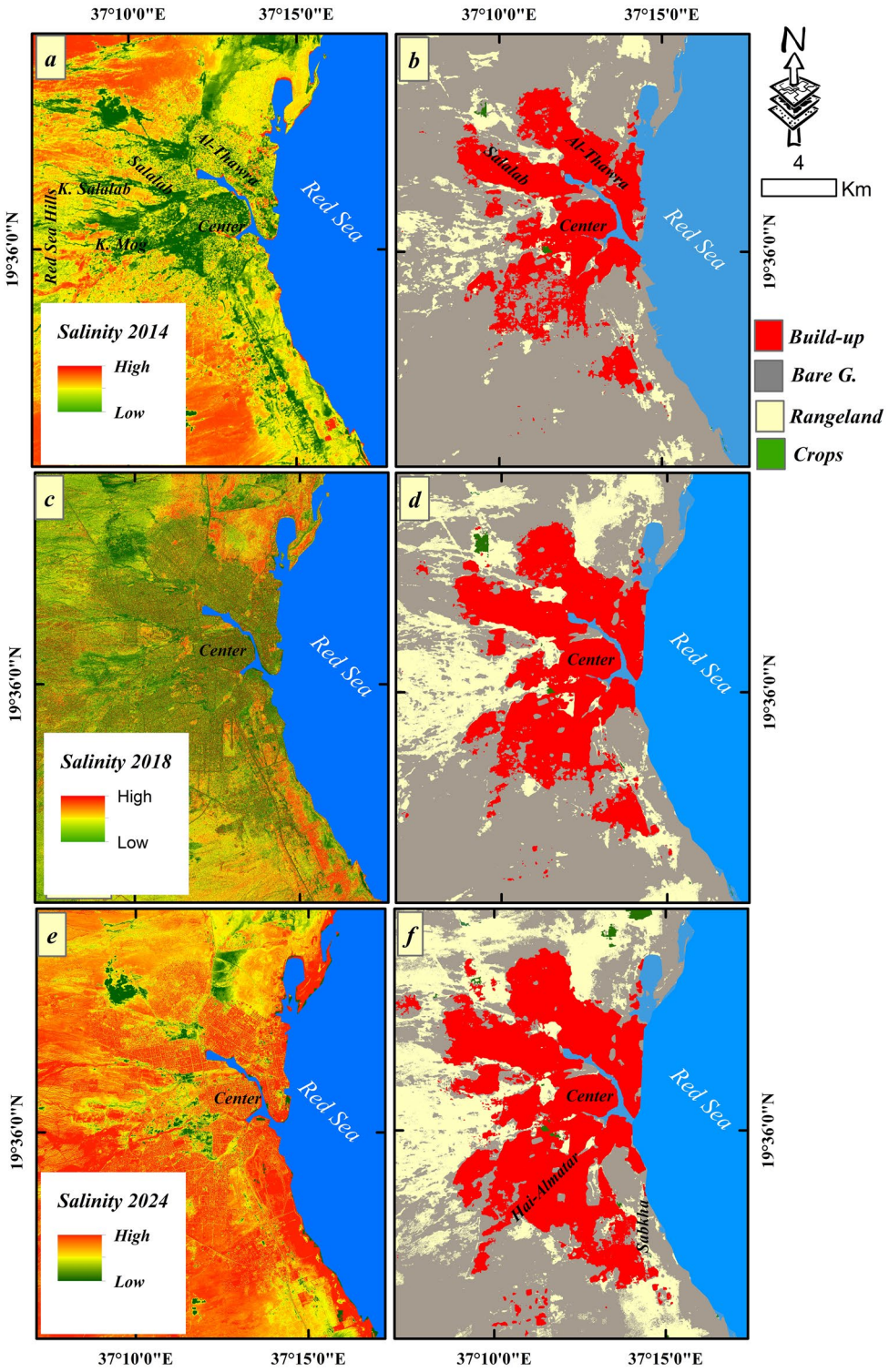

Fig. 11 Comparative maps illustrating the spatial correspondence between soil salinity and LULC change for 2014, 2018, and 2024. Panels (**a**, **c**, **e**) show satellite-derived SI distributions, while panels (**b**, **d**, **f**) depict corresponding LULC classifications for the same years highlighted zones where progressive urban expansion and land conversion coincide with increasing salinity intensity, particularly within reclaimed coastal areas, transportation corridors, and peri-urban districts

consistently coincide with coastal districts and expansion fronts, including Abu-Hashish, Salalab, Hai-Almatar, and newly developed infrastructure corridors (Fig. 14a–d). These patterns indicate that the conversion of bare ground to built-up and rangeland classes systematically shifts hydro-saline conditions inland, reinforcing the causal relationship between land-use transformation and soil degradation. The persistent spatial overlap of newly urbanized areas with elevated salinity and moisture demonstrates that surface sealing, drainage disruption, and altered runoff pathways are primary mechanisms influencing hydro-saline dynamics in Port Sudan.

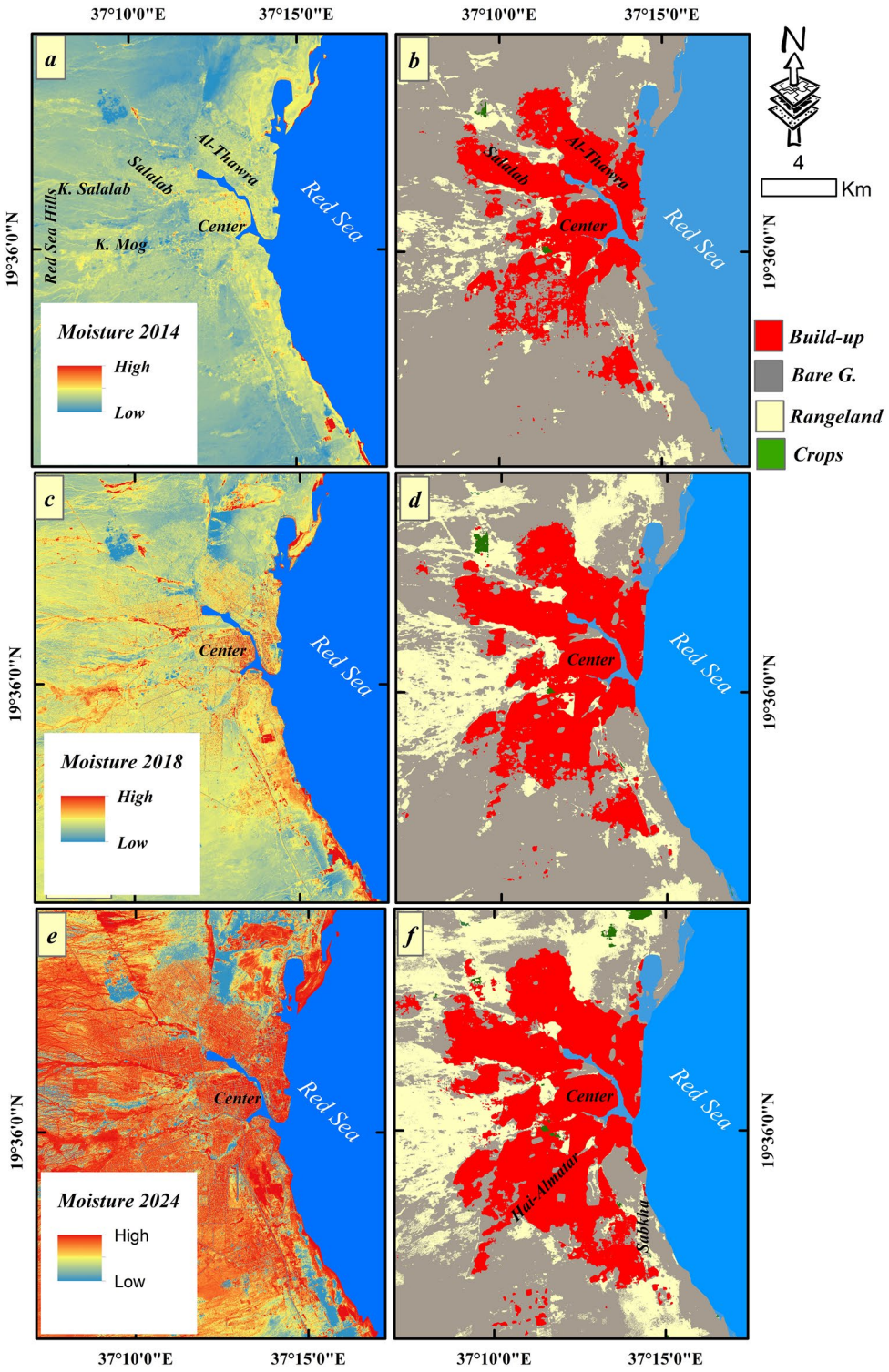

Fig. 12 Comparative maps showing the relationship between soil moisture distribution and LULC change for 2014, 2018, and 2024. Panels display satellite-derived SMI patterns (**a-c-e**) alongside corresponding LULC maps (**b-d-f**) for each year

4.4 Statistical Relationships Between LULC, Soil Salinity, and Moisture

Quantitative analysis of land use and land cover (LULC) change from 2008 to 2024 reveals a strong statistical association between landscape transformation and hydro-saline dynamics in Port Sudan. During this period, salinity-affected areas increased substantially from approximately 1.7 km^2 in 2008 to 87.6 km^2 in 2024, while moisture-affected areas expanded from a negligible extent to about 5 km^2 (see Table 2). These shifts coincided with the rapid growth of

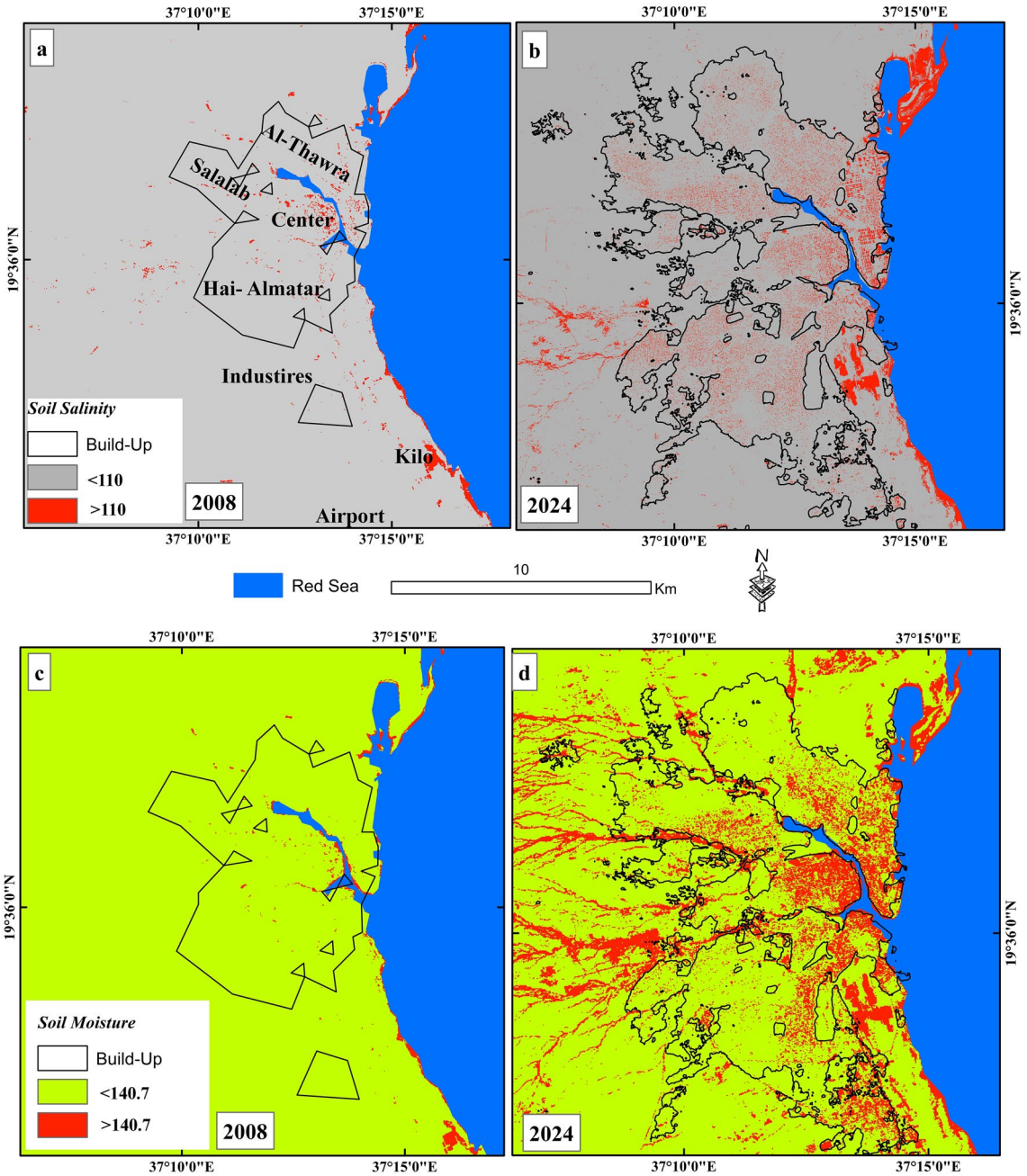

Fig. 13 Integrated spatial overlays of soil salinity of years (**a**) 2008; (**b**) 2024; and soil moisture with built-up areas for (**c**) 2008; (**d**) 2024, Red areas indicate pixels exceeding calibrated thresholds (SI > 110; SMI > 140), highlighting long-term inland expansion

built-up and peri-urban land cover, suggesting a direct relationship between urbanization and soil degradation.

Figure 15a shows that soil salinity is strongly and positively correlated with built-up area ($R^2 \approx 0.82$) and rangeland ($R^2 \approx 0.77$), and strongly and inversely correlated with bare ground ($R^2 \approx 0.81$). This pattern indicates that replacing naturally draining, barren surfaces with impervious or semi-impervious land cover alters surface runoff, reduces infiltration, and promotes salt accumulation in adjacent soils. Importantly, the scatter distribution in Fig. 15a indicates a non-linear response, whereby salinity increases modestly during early stages of urban expansion but rises disproportionately once built-up and rangeland coverage exceed a critical proportion of the landscape. This threshold-like behavior reflects cumulative disruption of drainage pathways and enhanced capillary-driven salt migration in shallow soils. The strong correlation with rangeland further suggests that peri-urban expansion into marginal lands contributes to salinization by disturbing shallow soils and enhancing upward salt transport.

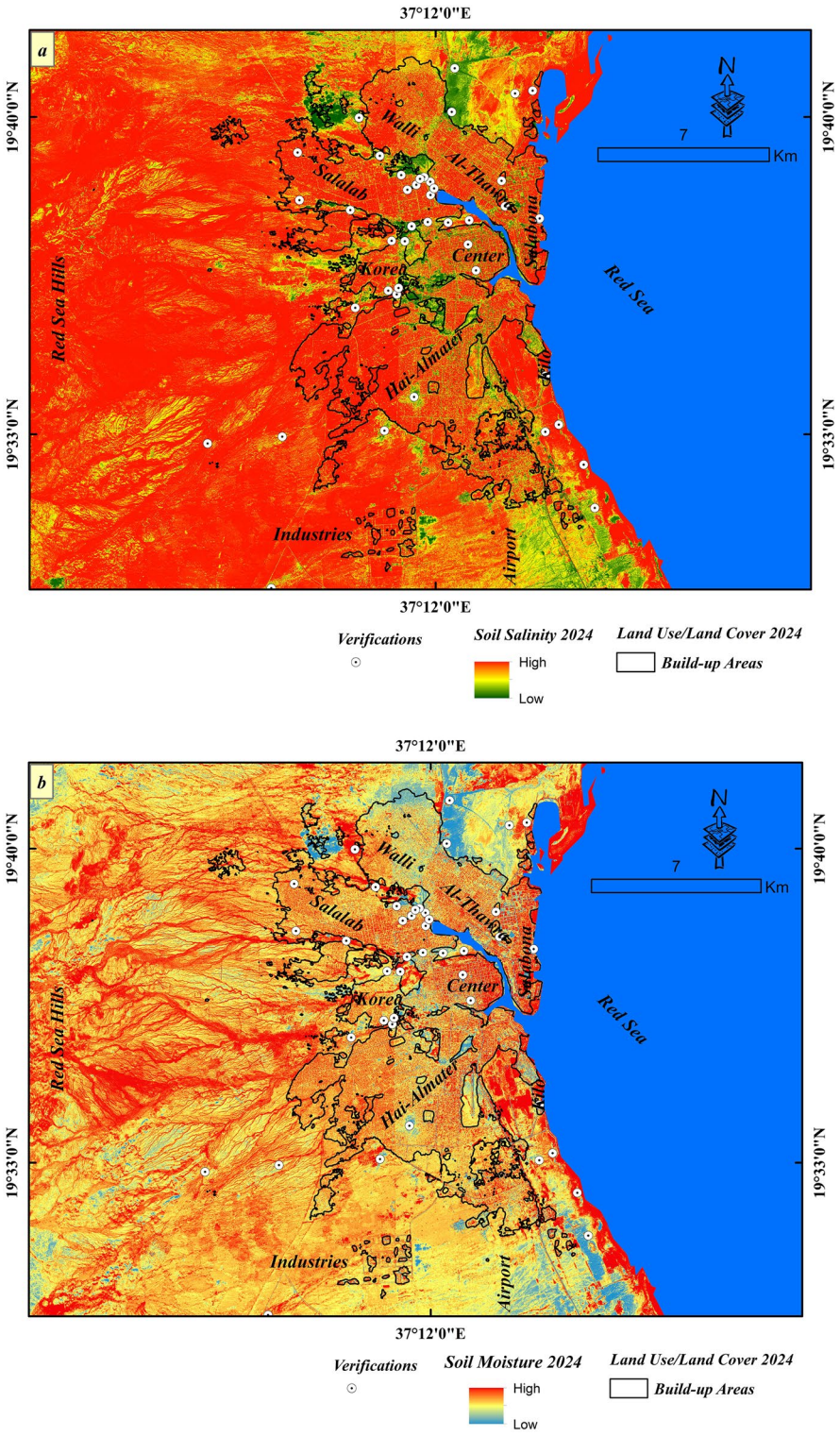

Fig. 14 Comparison of combined salinity and moisture intensity zones for the year 2024, illustrating strong spatial coupling between urban expansion and hydro-saline processes

In contrast, soil moisture demonstrates a moderate yet consistent correlation with built-up expansion ($R^2 \approx 0.63$; as summarized in Fig. 15b and Table 3). The comparatively weaker and more gradual response reflects the combined effects of episodic rainfall, localized water stagnation, shallow groundwater conditions, and partial masking of moisture signals beneath paved surfaces. Unlike salinity, moisture responds more gradually to land-cover change, increasing progressively rather than abruptly. Nevertheless, the positive correlation indicates that urban growth increases surface and near-surface water retention, especially in low-lying and reclaimed areas with limited drainage.

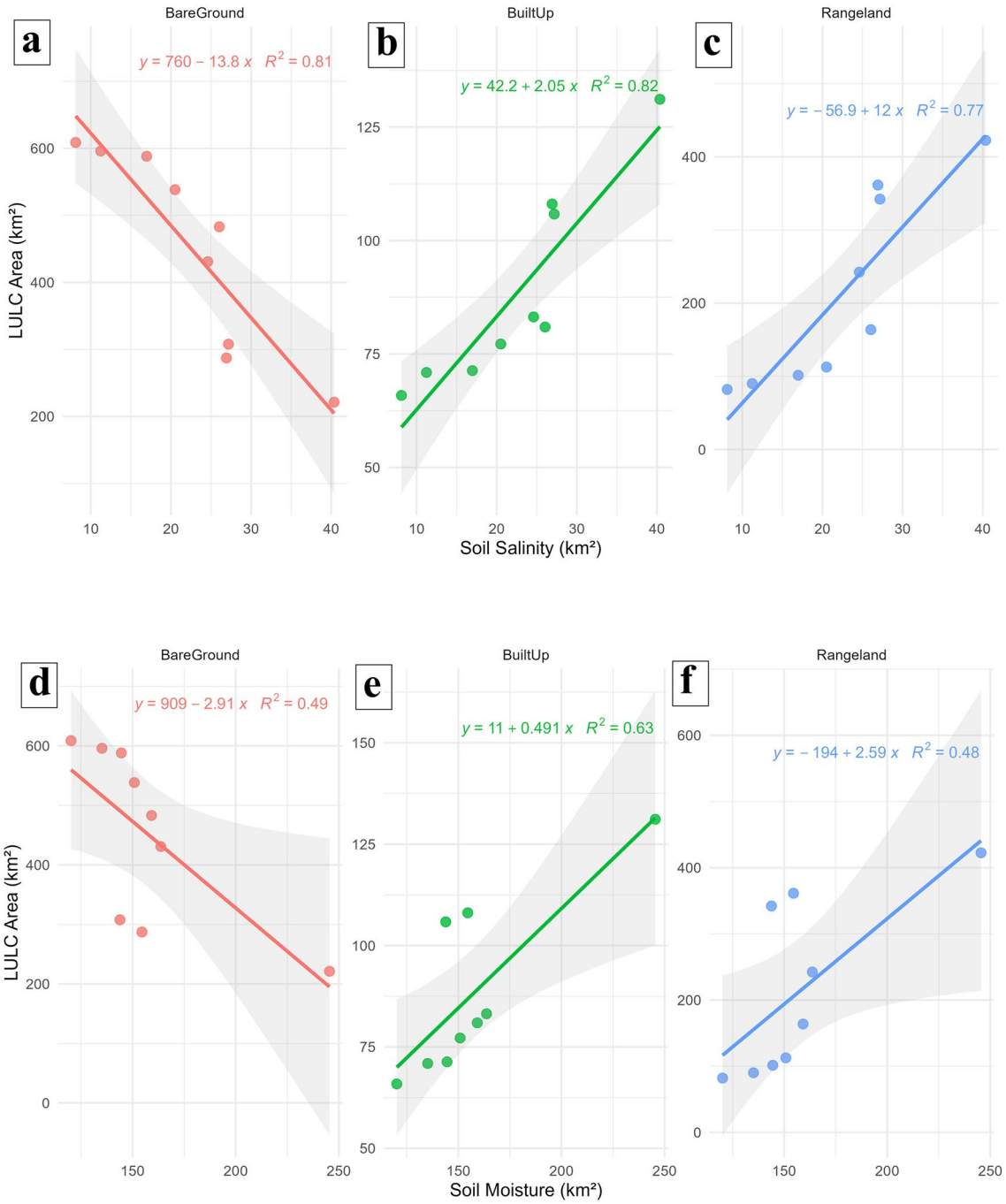

Fig. 15 Temporal relationships between soil salinity vs LULC parameters (**a**) bare ground; (**b**) build-up areas; (**c**) rangeland; (**d**) soil moisture relationship with (**d**) bare ground; (**e**) build-up areas; and (**f**) rangeland, showing statistically significant positive correlations between built-up expansion and hydro-saline intensification

Inter-LULC correlations further highlight the intensity of land conversion processes. Built-up area and rangeland display a very strong positive correlation ($R^2 \approx 0.94$), while bare ground shows a near-perfect inverse relationship with rangeland ($R^2 \approx 0.98$), confirming that urban and peri-urban expansion occurred predominantly at the expense of undeveloped barren land. These transitions fundamentally altered surface hydrological behavior, favoring moisture retention and salinity accumulation.

The correlation matrix (Fig. 16) supports these results, revealing a strong association between built-up area and salinity (r = 0.92) and a moderate-to-strong association with soil moisture (r = 0.73). The close relationship between salinity and moisture (r = 0.76) suggests that shallow

Table 3 Linear regression relationships between soil salinity, soil moisture, and LULC classes in Port Sudan (2008–2024)

Predictor Variable (km^2)	LULC Class	Regression Equation	R^2	Relationship	Remarks
Soil Salinity	Bare ground	$y = 760 - 13.8x$	0.81	Strong negative	Progressive loss of naturally draining barren surfaces reduces salt dispersion capacity
	Built-up	$y = 42.2 + 2.05x$	0.82	Strong positive	Expansion of impervious surfaces promotes salt accumulation through disrupted drainage
	Rangeland	$y = -56.9 + 12.0x$	0.77	Strong positive	Peri-urban land disturbance enhances shallow soil salinization
Soil Moisture	Bare ground	$y = 909 - 2.91x$	0.49	Moderate negative	Decline reflects conversion of open surfaces to partially sealed land cover
	Built-up	$y = 11 + 0.491x$	0.63	Moderate positive	Increased surface sealing and localized water stagnation enhance moisture retention
	Rangeland	$y = -194 + 2.59x$	0.48	Moderate positive	Soil disturbance and low drainage efficiency favor moisture accumulation

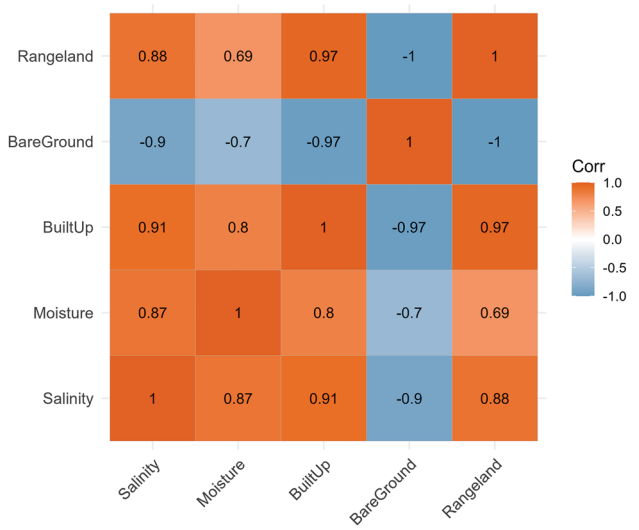

Fig. 16 Correlation heat-map illustrating relationships among LULC classes, soil salinity, and moisture across the study period

Table 4 Absolute and percentage changes of LULC and soil salinity and moisture from 2008 to 2024

Variable (km^2)	2008	2024	Absolute change km^2	Percent change
Built-up area	65.87	131.13	65.26	99.08
Bare ground	608.81	221.29	-387.53	-63.65
Rangeland	82.06	422.43	340.38	414.80
Soil salinity	8.12	40.36	32.24	397.04
Soil moisture	120.15	245.49	125.34	104.32
Water	254.98	255.18	0.20	0.08

groundwater rise and inefficient drainage in newly urbanized and reclaimed areas intensify salt accumulation. Spatial analysis using salinity and moisture maps (Figs. 9, 13, and 14) demonstrates that the most pronounced hydro-saline responses occur along reclaimed coastal zones, transportation corridors, and peri-urban expansion fronts. These findings provide consistent statistical and spatial evidence that urban expansion is a primary driver of hydro-saline intensification in Port Sudan.

Absolute and relative changes in land use and land cover, soil salinity, and soil moisture between 2008 and 2024 are summarized in Table 4 and visualized in Fig. 17 to synthesize the magnitude of landscape transformation and hydro-saline intensification. The findings indicate a substantial reorganization of the coastal urban system. Built-up areas nearly doubled, increasing by approximately 65 km^2 (about 99%), while bare ground declined by roughly 388 km^2 (about 64%), reflecting extensive conversion of naturally draining surfaces into urban and peri-urban (Fig. 17a and b). Rangeland experienced the largest proportional expansion, increasing by more than 340 km^2 (about 415%), suggesting outward urban and peri-urban growth into previously undeveloped terrain. These land transformations were accompanied by disproportionate increases in hydro-saline stress. Salinity-affected areas expanded from 8.12 km^2 to 40.36 km^2 representing an increase of nearly 400%, while moisture-affected areas more than doubled, increasing by approximately 125 km^2 (about 104%). In contrast, open water bodies exhibited negligible change (less than 0.1%), confirming that the observed trends are attributable to subsurface and near-surface hydro-saline processes rather than surface water expansion.

The relative increase in soil salinity is significantly greater than that of built-up areas, indicating a non-linear response of soil systems to urban expansion (Fig. 17c). This amplification results from the combined effects of increased surface sealing, altered runoff pathways, shallow saline

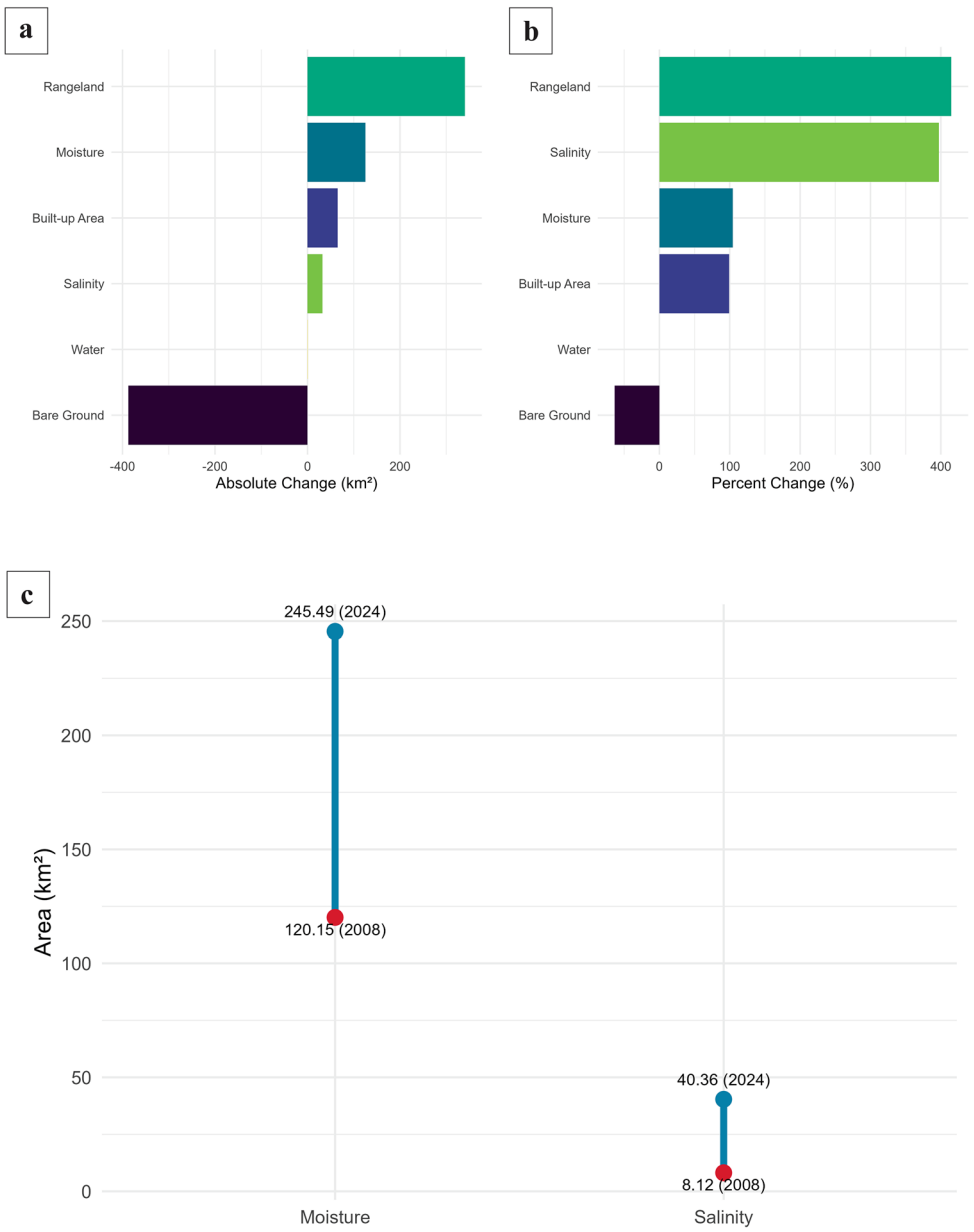

Fig. 17 Synthesis of (**a**) absolute; (**b**) relative changes in LULC; (**c**) salinity and moisture, highlighting the disproportionate amplification of hydro-saline stress relative to urban expansion

groundwater, and inefficient drainage in reclaimed and low-lying areas.

4.5 Implications for Built-Up Areas and Infrastructure Exposure

Field investigations in Port Sudan indicate that regions identified by remote sensing as hydro-saline hotspots consistently exhibit significant material deterioration and structural instability, particularly in low-lying sabkha terrain and reclaimed coastal zones. These environments are defined by sulfate- and chloride-rich evaporitic soils such as gypsum and halite, inadequate drainage, shallow saline groundwater, and pronounced capillary rise (Fig. 18a). Collectively, these conditions accelerate corrosion and reduce load-bearing capacity. The Salalab district (Fig. 18b) is among the most severely affected areas, where persistent waterlogging and saline groundwater are associated with elevated salinity and moisture indices. Extensive sabkha deposits cover much of the coastal plain (Fig. 18c), particularly in rapidly urbanizing and port-adjacent regions. In these environments, deterioration extends beyond buildings to include surrounding infrastructure such as pavements, boundary walls, and road shoulders, all of which display widespread cracking, deformation, and surface disintegration (Fig. 18d–e), consistent with prolonged hydro-saline stress.

At the material scale, reinforced concrete structures exhibit severe corrosion of steel reinforcement due to

Fig. 18 Field evidence of hydro-saline deterioration and structural distress in Port Sudan's coastal, reclaimed, and peri-urban zones, corresponding to salinity and moisture hotspots identified in satellite analysis. (**a**) Surface salt crusts and efflorescence developed on sabkha ground due to capillary rise and intense evaporation; (**b**) excavations exposing moist, saline–alkaline soils indicative of shallow groundwater and inefficient drainage; (**c**) widespread moisture discoloration and early-stage surface degradation affecting pavements and exposed ground; (**d-e**) reinforced concrete deterioration characterized by spalling (contour scaling) and loss of concrete cover, exposing corroded steel reinforcement; (**e**) lower-wall damage including efflorescence, blistering, and peeling of plaster associated with rising damp and salt crystallization; (**f-g**) foundation-level deformation expressed as cracking and differential settlement in low-lying structures; (**h-i**) advanced structural failure manifested as fragmentation and partial to complete collapse of buildings constructed on untreated hydro-saline ground

chloride and sulfate ingress (Fig. 18f–g). Repeated cycles of salt dissolution and crystallization generate crystallization pressures within pores and micro-fractures, resulting in progressive failure of protective coatings, plaster detachment, blistering, scaling, and ultimately spalling. The loss of concrete cover exposes reinforcement, thereby accelerating corrosion and structural degradation.

At the structural scale, prolonged exposure to salinity and moisture reduces soil strength and bearing capacity, resulting in differential settlement, foundation misalignment, and irregular cracking of walls and slabs (Fig. 18h). In severe cases, especially where construction was undertaken on untreated hydro-saline ground without sufficient geotechnical mitigation, partial to complete structural collapse has been documented in residential, industrial, and public buildings (Fig. 18i). The spatial representativeness of field observations is illustrated in Appendix A: Fig. 22, which shows the distribution of ground evidence across coastal, urban, reclaimed, and peri-urban zones.

These field observations correspond spatially to areas with high salinity and moisture indices in the L7/8/9 and S2 maps. Although impervious roofs and paved surfaces may locally suppress the surface spectral expression of salinity, salts accumulate in adjacent open strips and beneath foundations. This confirms that remote sensing detects the surface manifestation of a more extensive subsurface process.

4.6 Predictive Trends Under Continued Urban Growth (2008–2040)

Predictive analysis using ARIMA time-series modeling extends the observed LULC and hydro-saline trends from 2008–2024 to 2040 (Table 5). The forecasts indicate continued urban expansion, with built-up areas projected to exceed approximately 200 km^2 (≈20% of the total study

Table 5 Observed (2024) and forecasted (2030–2040) areal extents of major land-use/land-cover classes and hydro-saline processes, with associated 95% confidence ranges for 2040 projections

Variable	2024 Observed (km^2)	2030 Forecast (km^2)	2040 Forecast (km^2)	95% Confidence Range (2040)
Built-up Area	131.13	160.50	195.00	180–210
Bare Ground	221.29	170.00	120.00	100–140
Rangeland	422.43	450.00	480.00	460–510
Soil Salinity	40.36	85.00	150.00	135–165
Soil Moisture	245.49	280.00	320.00	300–340

area) by 2040 (Fig. 19a). In contrast, bare ground is expected to decline below 150 km^2 (Fig. 19b), while rangeland may expand beyond 500 km^2, reflecting sustained land-use redistribution associated with urban expansion and peripheral landscape transformation (Fig. 19c). Environmental projections show a parallel intensification of hydro-saline conditions. Areas affected by elevated soil salinity are projected to surpass 150 km^2 by 2040 (Fig. 19d), while soil moisture exhibits a persistent upward trend, reaching approximately 300–340 km^2 within the 95% confidence intervals (Fig. 19e). These trajectories indicate that salinity expansion is more spatially extensive than the increase in moisture, but both variables continue to respond positively to ongoing land-use transformation.

The ARIMA forecasts assume continuation of recent growth rates and do not explicitly account for future changes in population dynamics, economic activity, or mitigation measures (see Appendix C: Tables 11 and 12). Accordingly, the projections should be interpreted as potential trajectories rather than deterministic outcomes, highlighting the direction and relative magnitude of change under prevailing development patterns.

5 Discussion

5.1 Urbanization–Hydro-Saline Feedbacks in Arid Coastal Region

The multi-temporal geospatial analysis conducted in this study reveals clear and evolving relationships among LULC dynamics, soil salinity, and soil moisture patterns in Port Sudan over the period from 2008 to 2024. The findings point to a strong spatial and temporal correlation between urban expansion and increased environmental stress, particularly in terms of salinity intrusion and soil moisture accumulation, especially, the expansion of built-up areas, especially between 2018 and 2024, appears to be a major driver of salinity and moisture variability (Daoud et al. 2025; Hawash et al. 2021). High-resolution salinity maps derived from S2 imagery identified distinct zones of elevated salinity between paved roads and adjacent buildings. While roads and rooftops themselves showed low salinity values due to their impermeable surfaces, these paved structures alter the natural hydrological flow, leading to localized salt accumulation in the unpaved strips between them. This phenomenon is exacerbated by shallow saline groundwater and the widespread use of desalinated water in households, where concentrated brine effluents are often discharged

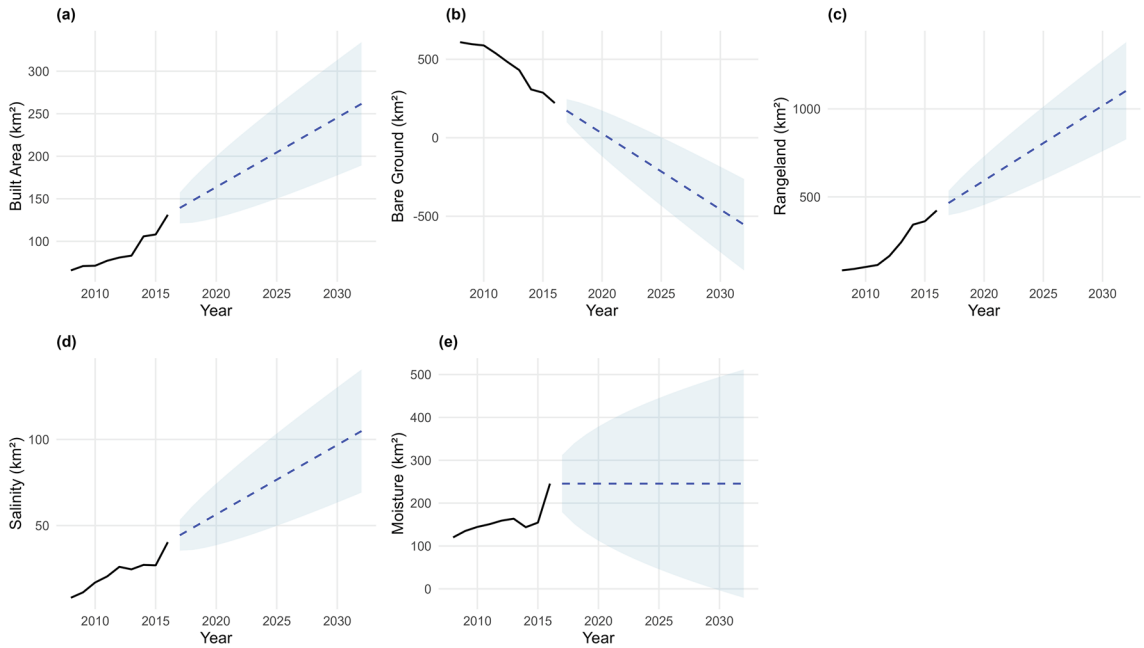

Fig. 19 Time series forecasting to 2040 for (**a**) built-up area; (**b**) bare ground; (**c**) rangeland; (**d**) soil salinity; and (**e**) soil moisture. Projections represent the continuation of observed trends under current land-use trajectories and are not deterministic forecasts

into the ground. Such practices contribute significantly to salt buildup in urban soils (Thiam et al. 2021; Zeyada et al. 2023).

The apparent mismatch between remotely sensed surface salinity and actual structural deterioration observed in the field further emphasizes the need for integrated analysis (Daoud et al. 2025; Dinnat et al. 2019; Reul et al. 2020). Buildings that appeared unaffected in satellite imagery were, in fact, exhibiting signs of material degradation, including corrosion of steel reinforcements, foundation erosion, wall cracking, and surface scaling (see Figs. 13 and 15). These damages are most prominent in districts with poor drainage and persistent waterlogging, where saline water interacts chemically with construction materials. Field surveys confirmed that 24 districts (see Fig. 1b), including Center, Hai-Almatar Salalab, Al-Thawra, and Abu-Hashish are high-vulnerability zones for construction due to a combination of elevated soil salinity, high moisture retention, and inadequate infrastructure planning.

5.2 Linking Remote-Sensing Indicators with Field-Observed Infrastructure Deterioration

Field surveys confirm that areas identified by satellite analysis as hydro-saline affected correspond to zones of active material deterioration and geotechnical instability. In Port Sudan sub-districts such as Salalab, Alsouq Alshaabi, and peri-urban industrial zones, shallow saline groundwater combined with persistent moisture enhances capillary rise and evaporite accumulation. These processes are expressed in the field as salt crusts, efflorescence, damp bands, and prolonged waterlogging, consistent with deterioration patterns defined by (Vergès-Belmin 2008).

At the material and structural scale, repeated salt dissolution–crystallization cycles accelerate degradation of construction materials, progressing from surface peeling and blistering to scaling, concrete spalling, reinforcement corrosion, cracking, differential settlement, and, in severe cases, partial or total structural collapse (Nguyen et al. 2024; Rijniers et al. 2005; Yang et al. 2025; Zhang et al. 2024) (see Fig. 15). The spatial coincidence between these damage patterns and satellite-derived zones of high salinity and moisture confirms the relevance of remote sensing for identifying infrastructure risk areas. However, field evidence also shows that subsurface salinity and moisture can continue to degrade foundations even where paved surfaces obscure surface expressions, reflecting the hydrologic impacts of urban impervious cover (Weng 2012). Similar hydro-salinity–driven deterioration mechanisms have been reported in other arid coastal cities built on sabkha and reclaimed land, reinforcing the broader applicability of these findings (Hou and Rusuli 2022; Jamali et al. 2020; Saad et al. 2024). While satellite indices primarily capture surface expressions, field evidence demonstrates that subsurface salinity and moisture continue to affect foundations even where rooftops and asphalt mask the surface reflectance.

5.3 LULC Controls on Salinity and Moisture Dynamics

Statistical analysis confirms that land-use transformation is tightly linked to environmental degradation. The strong positive correlations between built-up expansion and salinity ($r \approx 0.82$) and moisture ($r \approx 0.76$), together with the strong negative relationship between bare ground and both parameters (see Fig. 15a-b), demonstrate that replacing natural, permeable surfaces with impervious or semi-pervious land covers fundamentally alters soil–water interactions. Rangeland expansion, often occurring at the urban fringe, also shows a positive association with salinity and moisture. This reflects conversion of marginal lands underlain by shallow groundwater, where grazing areas often lack drainage infrastructure and become secondary accumulation zones. In contrast, undeveloped barren areas away from urban influence consistently exhibit lower salinity and moisture, underscoring the dominant role of anthropogenic modification over regional climate alone.

5.4 Integrated Interpretation: Environmental Implications for Coastal Urban Systems

The integrated interpretation of LULC, soil salinity, and soil moisture dynamics highlights a complex interaction between human-induced urbanization and natural coastal processes in Port Sudan. The observed spatiotemporal patterns suggest that urban expansion has contributed to the coastal hydro-salinization balance, intensifying salt migration, surface water retention, and subsurface degradation. These processes are driven by the proliferation of impervious surfaces, reduced infiltration capacity, and the rerouting of natural drainage systems, collectively disturbing the equilibrium among soil, groundwater, and surface hydrology. Consequently, built-up areas have become both agents and victims of salinization promoting conditions that degrade their own structural foundations.

From an environmental perspective, these findings underscore the vulnerability of arid coastal cities where rapid urban development intersects with fragile geomorphological settings (Abd El-Hamid et al. 2023; Nguyen et al. 2024). Port Sudan's coastal corridor, underlain by shallow saline groundwater and sabkha deposits, is particularly sensitive to anthropogenic modification. The conversion of natural sabkha and bare ground into urban zones has not only reduced natural drainage but also enhanced capillary

salt rise and surface crusting. Over time, such changes can lead to secondary salinization of surrounding ecosystems, with consequences for vegetation health, soil fertility, and biodiversity in adjacent rangelands and peri-urban areas (see Fig. 15).

The urban-environmental feedback observed here also carries important implications for infrastructure sustainability. Structural degradation, such as corrosion, cracking, and foundation instability, is not merely a result of surface salinity but reflects deeper hydrological and geochemical transformations in the subsurface environment. The coexistence of elevated soil moisture and salinity amplifies deterioration rates of construction materials, shortening the service life of roads, buildings, and drainage systems (Yang et al. 2025; Zhang et al. 2024). Without adequate mitigation, these conditions may escalate maintenance costs and limit the longevity of newly developed urban sectors. In dense urban environments, direct assessment of subsurface soil conditions beneath buildings is not feasible using optical satellite data alone. In this study, hydro-saline conditions beneath built-up areas are not assumed directly but are inferred from spatially adjacent exposed soils, transitional strips between buildings and roads, shallow groundwater conditions, and consistent field evidence of material degradation (e.g., corrosion, efflorescence, foundation cracking). This inference is supported by the continuity of soil units, shallow groundwater depths, and capillary-driven salt migration typical of sabkha and reclaimed coastal settings.

At a broader scale, the Port Sudan case exemplifies challenges common to many coastal urban systems in arid regions. Climate variability, rising sea levels, and increased reliance on desalinated water (with brine discharge into the ground) compound local salinization processes. Integrated management approaches linking remote sensing, hydrological modeling, and urban planning are therefore essential for designing adaptive infrastructure and sustainable land use strategies. Implementing green infrastructure, improving drainage efficiency, and enforcing urban zoning regulations that account for subsurface salinity exposure could significantly mitigate future degradation.

5.5 Limitations and Future Considerations

Although this multi-temporal geospatial analysis provides important insights, several limitations must be acknowledged when interpreting the results. The multi-year satellite archive facilitates the assessment of spatiotemporal trends; however, the limited number of observation dates restricts the robustness of long-term predictive modeling. Sparse temporal sampling increases uncertainty in trend extrapolation and diminishes the reliability of advanced forecasting methods, which require dense and continuous time series. Consequently, the ARIMA-based projections should be interpreted as indicative trajectories under current land-use and environmental conditions rather than as deterministic forecasts.

A significant methodological limitation involves the scale dependency and physical interpretation of satellite-derived salinity and moisture indices. Optical indices primarily capture relative surface conditions and are highly sensitive to sensor spatial resolution and land-cover heterogeneity. In densely built urban environments, impermeable materials such as asphalt and concrete obscure soil exposure and reduce the spectral expression of saline and moisture-affected substrates. Mixed-pixel effects at coarser spatial resolutions, particularly in Landsat imagery, further weaken localized hydro-saline signals by integrating multiple surface types within individual pixels. While the higher spatial resolution of Sentinel-2 improves the delineation of salinity and moisture patterns, under-representation persists in compact urban cores where exposed soil is limited and shadowing effects are substantial. Field calibration indicates that these effects are most pronounced in dense built-up areas, whereas correspondence between satellite indices and ground observations improves in open and peri-urban zones with greater soil exposure. Employing Landsat for temporal continuity, Sentinel-2 for spatial refinement, and targeted field surveys mitigate but do not eliminate scale-related uncertainty. This confirms that remote sensing slightly under-represents hydro-saline severity in dense urban cores, a limitation explicitly acknowledged and mitigated through targeted field verification, while optical data can capture surface patterns and can improve subsurface salinity and moisture estimation (Chaaou et al. 2025).

A further limitation arises from the semi-quantitative nature of the salinity and moisture indices employed. These indices are unitless and reflect relative intensity rather than absolute physical parameters such as electrical conductivity or volumetric water content. Although classification thresholds were calibrated using field-verified salt-affected sites, ground measurements were collected infrequently and do not fully capture the temporal variability present in the satellite record. Consequently, the resulting maps should be interpreted as relative indicators of hydro-saline stress rather than as laboratory-equivalent measurements, which restricts direct comparison with standard soil salinity classifications used in agronomic or geotechnical contexts. Converting these indices into quantitative estimates would require systematic, multi-season field sampling, laboratory analyses, and the development of empirical or data-driven calibration models that integrate spectral, thermal, and terrain variables. Incorporating complementary datasets, such as SAR-based moisture proxies or near-surface geophysical conductivity measurements, could further enhance

sensitivity to subsurface salinity that optical sensors cannot detect beneath sealed urban surfaces.

Future studies should integrate detailed geotechnical and geochemical investigations to quantify subsurface salinity beneath built-up areas, including borehole-based soil sampling, laboratory analyses of soluble salts (Cl^-, SO_4^{2-}, Na^+, Mg^{2+}), cation exchange capacity in clay-rich layers, and continuous groundwater EC monitoring. Such data would allow direct validation of remotely inferred hydro-saline conditions and improve engineering design criteria for foundations and infrastructure in coastal urban environments. Coupling these measurements with geophysical methods (e.g., electrical resistivity tomography) and SAR-based moisture proxies would further enhance subsurface characterization beneath impervious surfaces.

Additional constraints stem from limited environmental monitoring infrastructure and restricted access to long-term soil and hydrological datasets, which have impeded extensive validation and continuous calibration. Future research should prioritize expanding temporal and spatial monitoring, integrating laboratory-based measurements, and strengthening institutional collaboration to improve quantitative accuracy and support sustainable urban planning in arid coastal environments such as Port Sudan.

6 Conclusion

This study presents a comprehensive assessment of the evolving impacts of soil salinity and moisture on the urban landscape and infrastructure of Port Sudan from 2008 to 2024, utilizing remote sensing, GIS-based multi-temporal analysis, and detailed field-based structural assessments. The findings indicate a strong and intensifying relationship between rapid urban expansion and hydro-saline degradation in arid coastal environments. Newly urbanized areas, reclaimed coastal lands, and peri-urban rangelands show significant increases in both salinity and moisture, primarily due to shallow saline groundwater, disrupted drainage, and the proliferation of impervious surfaces.

High-resolution Sentinel-2 analyses demonstrate that hydro-saline affected areas extend beyond traditional sabkha zones to include narrow transitional strips between roads and building areas, which are particularly susceptible to subsurface salinity accumulation despite limited surface spectral signals. Field observations corroborate that these conditions lead to significant impacts on infrastructure, including foundation settlement, wall cracking, corrosion of steel reinforcement, and progressive concrete deterioration. Statistical analyses further support these findings, revealing strong positive correlations between built-up expansion and salinity ($r=0.82$) and moisture ($r=0.76$), as well as a marked negative relationship between urban growth and bare ground ($r=-0.81$).

Time-series modeling suggests that, if current development patterns continue, urban expansion and associated hydro-saline stress will likely intensify through 2040, especially in low-lying and reclaimed coastal sectors. These trends have significant implications for the long-term sustainability of infrastructure, urban resilience, and environmental health in Port Sudan and comparable arid coastal cities. The identified feedback loop among land-use transformation, salinization, and moisture retention underscores the necessity for integrated planning strategies that include soil and groundwater monitoring, enhanced drainage design, and construction practices that account for salinity risks.

Future research should emphasize more frequent temporal monitoring, multi-season field measurements of electrical conductivity and soil moisture, and the integration of complementary datasets, including SAR-based moisture indicators and near-surface geophysical surveys, to improve subsurface detection. Incorporating machine learning, deep learning, and process-based hydrological models, supported by expanded ground calibration, would further enhance predictive capabilities. This study establishes a transferable, field-calibrated framework for assessing hydro-saline risks in rapidly urbanizing arid coastal environments and offers a scientific foundation for risk-informed urban planning, climate adaptation, and sustainable infrastructure management.

Appendix A

Soil Salinity and Moisture Calculation

See Tables 6, 7 and 8, Figs. 20, 21 and 22.

Table 6 Indices calculation

Index	Purpose	Formula	Required Bands / Parameters
NDVI	Vegetation masking & emissivity	(NIR − Red)/(NIR + Red)	Red, NIR
NDMI	Surface moisture (Landsat)	(NIR − SWIR)/(NIR + SWIR)	NIR, SWIR
NDWI	Surface moisture (Sentinel-2)	(Green − NIR)/(Green + NIR)	Green, NIR
SI	Soil salinity intensity	(SWIR1* Red)/Blue	Red, Green, Blue
PV	Fractional vegetation	$((NDVI - NDVImin)/(NDVImax - NDVImin))^2$	NDVI
LSE	Surface emissivity	0.004 × PV + 0.986	PV
LST	Surface temperature	see Eq. (6–7)	Thermal bands
SMI	Relative soil moisture	(LSTmax − LST)/(LSTmax − LSTmin)	LST

Table 7 VES datasets used to calculate threshold obtained from Electrical Resistivity carried using Winner method to detect and calculate near surface soil salinity

ID	North	East	Resistivity (Ω·m)	Conductivity (Mhos/m)	EC (mS/cm)
VES1	19.74774	37.25925	2.56E+01	3.91E−02	3.91E+00
VES2	19.73559	37.21418	1.25E+02	8.00E−03	8.00E−01
VES3	19.73573	37.17552	1.19E+01	8.40E−02	8.40E+00
VES4	19.72810	37.13400	1.22E+02	8.20E−03	8.20E−01
VES5	19.68287	37.21013	2.73E+00	3.66E−01	3.66E+01
VES6	19.67175	37.16613	7.22E+01	1.39E−02	1.39E+00
VES7	19.67000	37.13000	2.37E+00	4.22E−01	4.22E+01
VES8	19.53899	37.23901	1.27E+00	7.87E−01	7.87E+01
VES9	19.63039	37.21149	5.54E−01	1.81E+00	1.81E+02
VES10	19.62000	37.19000	1.94E+01	5.15E−02	5.15E+00
VES11	19.61782	37.12820	1.72E+02	5.81E−03	5.81E−01
VES12	19.54288	37.17534	2.11E+02	4.74E−03	4.74E−01
VES13	19.55938	37.21960	2.42E+02	4.13E−03	4.13E−01
VES14	19.55000	37.20000	2.13E+02	4.69E−03	4.69E−01
VES15	19.56306	37.23847	1.67E+00	5.99E−01	5.99E+01
VES16	19.50000	37.26000	3.11E+00	3.22E−01	3.22E+01
VES17	19.46452	37.27729	2.97E+00	3.37E−01	3.37E+01
VES18	19.50844	37.24215	1.38E+02	7.25E−03	7.25E−01
VES19	19.49900	37.22422	2.57E+02	3.89E−03	3.89E−01
VES20	19.49253	37.20002	1.88E+02	5.32E−03	5.32E−01
VES21	19.46388	37.26455	6.98E+01	1.43E−02	1.43E+00
VES22	19.46413	37.24377	1.44E+01	6.94E−02	6.94E+00
VES23	19.45451	37.22083	5.05E+01	1.98E−02	1.98E+00
VES23	19.45451	37.22083	5.05E+01	1.98E−02	1.98E+00
VES24	19.45711	37.23018	3.03E+01	3.30E−02	2.11E+00

Table 8 Threshold calculation based on selective representative EC of the soil from field observations using VES

ID	North	East	Salinity Value from Raster	Conductivity dS/m	Threshold	Threshold Percent
VES1	19.748	37.259	1.02	0.14	67.00	26.27
VES17	19.465	37.277	1.03	0.19	2.00	0.78
VES5	19.683	37.210	1.02	0.36	50.00	19.61
VES16	19.500	37.260	1.03	0.50	48.00	18.82
VES8	19.539	37.239	1.03	0.77	78.00	30.59
VES15	19.563	37.238	1.04	0.78	29.00	11.37
VES9	19.630	37.211	1.02	0.94	32.00	12.55
S1	19.485	37.281	1.80	17.00	183.00	71.76
S2	19.506	37.267	1.47	20.00	255.00	100.00
S3	19.512	37.269	1.52	19.00	220.00	86.27
RS1	19.609	37.242	1.19	17.00	236.00	92.55
RS2	19.603	37.236	1.34	18.00	245.00	100.00
Calculated Threshold in our study area					110.00	43.14

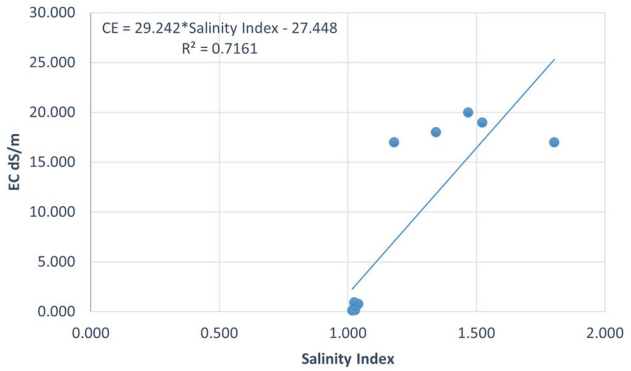

Fig. 20 Regression analysis between the calculated SI and ground validation EC, demonstrating the performance of the salinity estimation approach

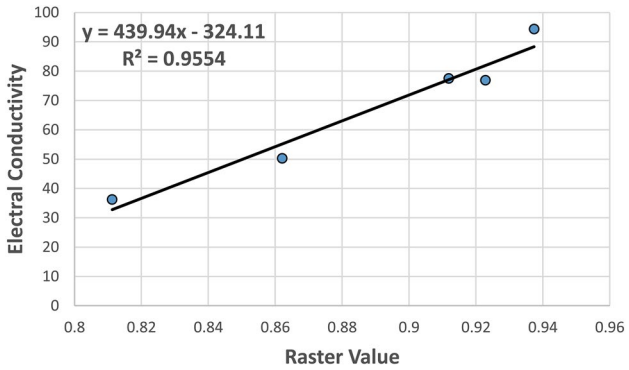

Fig. 21 Regression analysis illustrating the relationship between the satellite-derived Soil SI and ground-measured EC at independent validation checkpoints. These checkpoints were not incorporated in model development or calibration and were used exclusively for final validation and verification of the salinity estimation approach

Fig. 22 Spatial distribution of field observation sites used to validate satellite-derived salinity and moisture patterns in Port Sudan. The central map shows the locations of representative field observations (**a**–**p**) across coastal sabkha, reclaimed land, urban core, and peri-urban zones. Insets illustrate corresponding field conditions, including surface salt crusts, waterlogging, saline–alkaline soils, corrosion of reinforced concrete, cracking, and structural failure. Locations coincide with high salinity (SI > 110) and moisture (SMI > 140) zones identified in remote sensing analysis, supporting the spatial representativeness of field validation

Appendix B

Multi-Sensor Detection of Salinity and Moisture Dynamics (2008–2024)

See Figs. 23, 24 and 25.

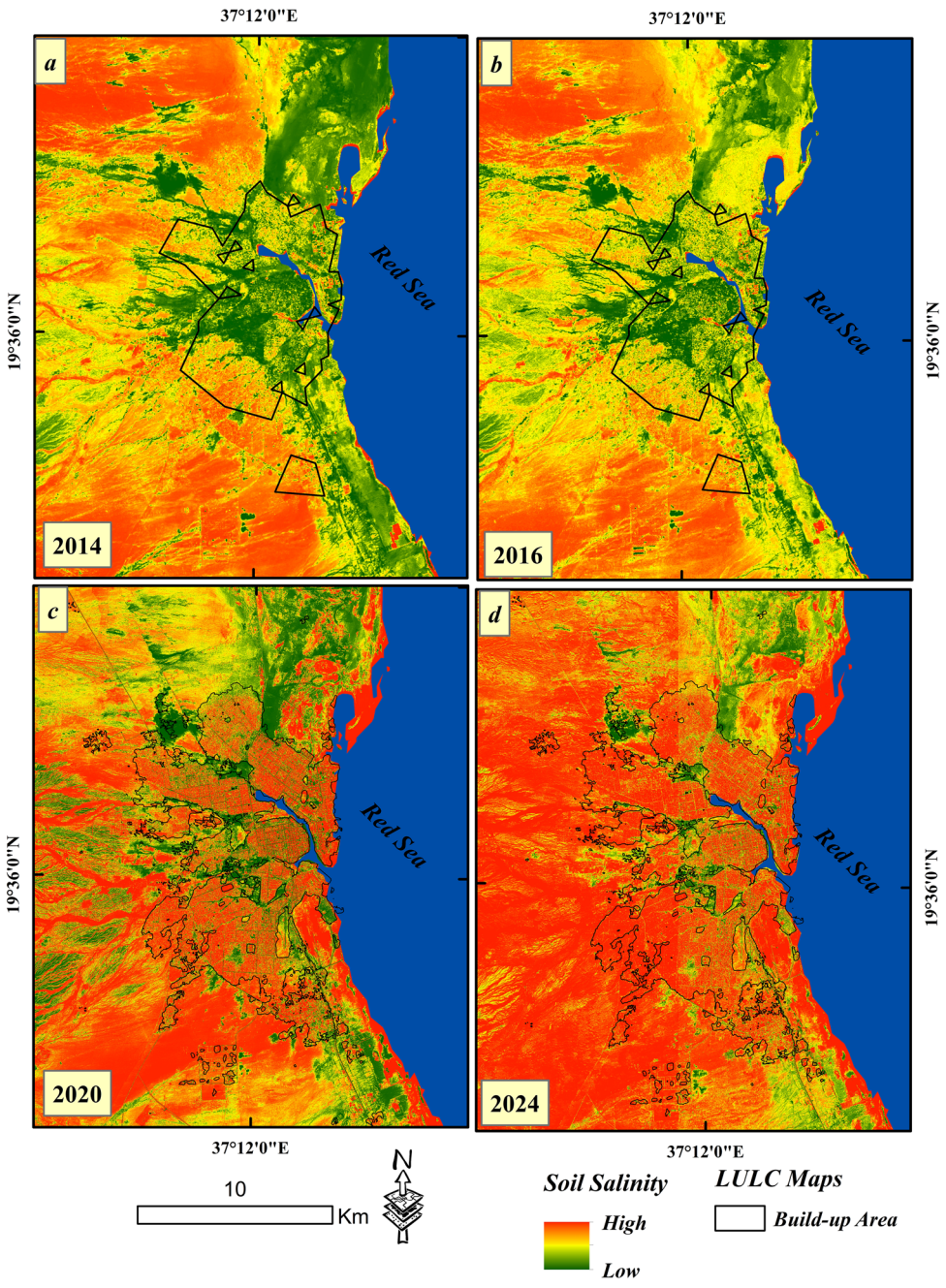

Fig. 23 Multi-temporal soil salinity distribution in Port Sudan derived from Landsat-7/8/9 salinity indices for (**a**) 2014 and (**b**) 2016, and from Sentinel-2 data for (**c**) 2020 and (**d**) 2024. All maps are displayed using a fixed color scale to enable direct temporal comparison, where red indicates high soil salinity and green represents low salinity levels

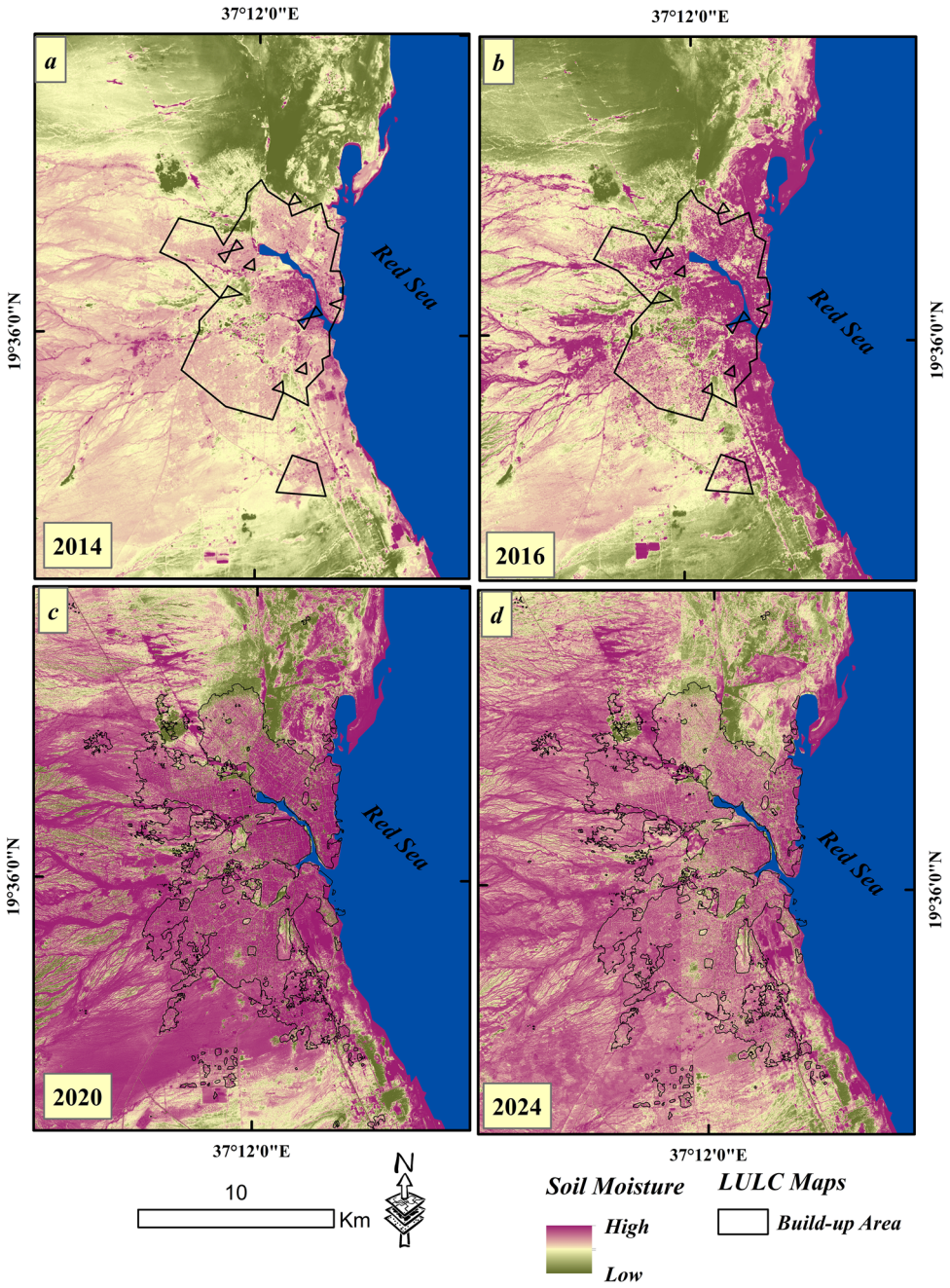

Fig. 24 Multi-temporal soil moisture distribution in Port Sudan derived from Landsat-7/8/9 data for (**a**) 2014 and (**b**) 2016, and from Sentinel-2 imagery for (**c**) 2020 and (**d**) 2024. All maps are displayed using a fixed color scale to facilitate direct temporal comparison, where purple indicates areas of high soil moisture and dark green indicates low moisture conditions

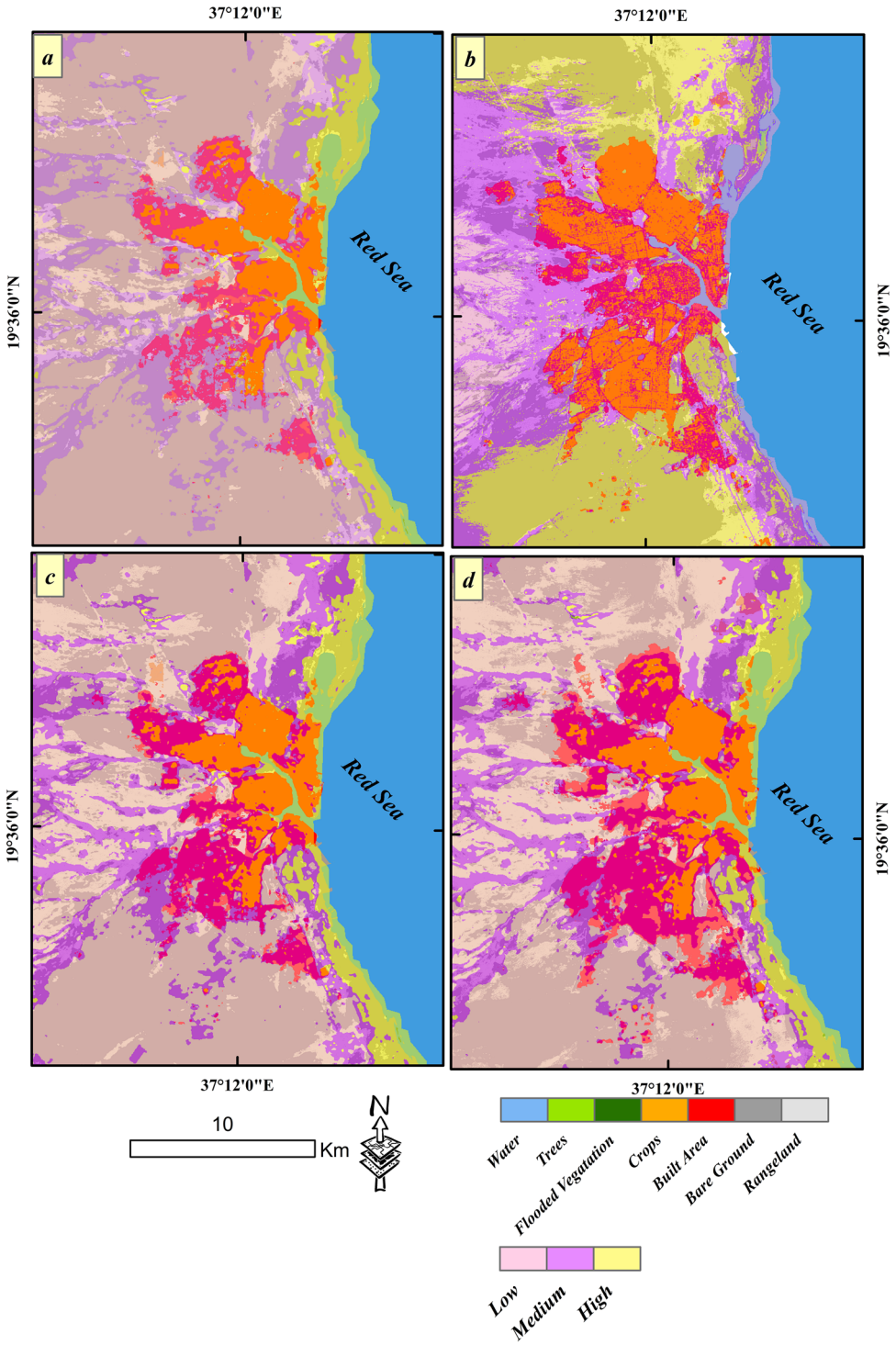

Fig. 25 Spatial distribution maps indicating changes in soil salinity and soil moisture from 2014 to 2024 in relation to built-up area expansion

Appendix C

Predictive Trends of LULC, Soil Salinity, and Moisture (2008–2040)

See Tables 9, 10, 11 and 12, Figs. 26, 27.

Table 9 LULC percentage changes in Port Sudan city from 2008 to 2024 (%)

Year	Crops	Built-Up	Bare-Ground	Rangeland
2008	0.01	8.71	80.42	10.86
2010	0.04	9.37	78.70	11.89
2012	0.07	9.37	77.25	13.32
2014	0.01	10.19	71.00	18.80
2016	0.04	11.10	66.34	22.52
2018	0.07	11.14	57.72	31.07
2020	0.16	13.93	40.51	45.40
2022	0.08	14.32	38.15	47.45
2024	0.29	16.89	28.48	54.34

Table 10 Area estimates (km^2) of soil salinity, soil moisture, and land-use/land-cover classes for the analyzed years

Year	Salinity	Moisture	Built-Up	Bare ground	Rangeland	Water
2008	8.12	120.15	65.87	608.81	82.06	254.98
2010	11.24	135.12	70.93	595.96	90.05	254.57
2012	16.97	144.50	71.33	588.17	101.38	254.88
2014	20.51	150.84	77.20	538.39	112.62	254.78
2016	26.04	159.17	80.95	483.04	163.71	254.88
2018	24.6	163.67	83.17	430.93	242.33	255.48
2020	27.18	143.86	105.84	307.80	342.10	254.98
2022	26.92	154.54	108.06	287.26	361.32	254.88
2024	40.36	245.49	131.13	221.29	422.43	255.18

Table 11 ARIMA model diagnostics for soil salinity and soil moisture time series, reporting estimated parameters, residual variance (σ^2), log-likelihood, and information criteria (AIC, AICc, and BIC)

sigma^2 = 38.76: log likelihood = -19.49
AIC = 40.97 AICc = 41.97 BIC = 40.76
= = = ARIMA MOISTURE = = =
Series: ts_data
ARIMA(0,0,0) with non-zero mean
Coefficients:
Mean
166.01
s.e. 12.523
sigma^2 = 1281: log likelihood = -34.44
AIC = 72.87 AICc = 75.87 BIC = 72.76

* While the ARIMA model captures long-term tendencies, it does not explicitly incorporate socio-economic or climatic drivers, and therefore the projections represent statistical extrapolations rather than deterministic forecasts

Table 12 Combined point forecasts and uncertainty ranges for built-up area, soil salinity, and soil moisture

Variable	Forecast Step	Point Forecast (km^2)	80% CI (Lo–Hi)	95% CI (Lo–Hi)
Built-up area	Early	139.29	127.45–151.13	121.18–157.40
	Mid	196.39	162.90–229.89	145.17–247.62
	Late	261.66	214.29–309.02	189.22–334.10
Soil salinity	Early	44.39	38.55–50.23	35.46–53.32
	Mid	72.60	56.09–89.11	47.35–97.85
	Late	104.84	81.49–128.19	69.14–140.54
Soil moisture	Early	245.49	201.98–289.00	178.95–312.03
	Mid	245.49	122.43–368.55	57.29–433.69
	Late	245.49	71.46–419.52	−20.67–511.65

Projected areal extents (km^2) with associated 80% and 95% confidence intervals derived from time-series forecasting. Values illustrate contrasting trend behaviors and increasing uncertainty with forecast horizon

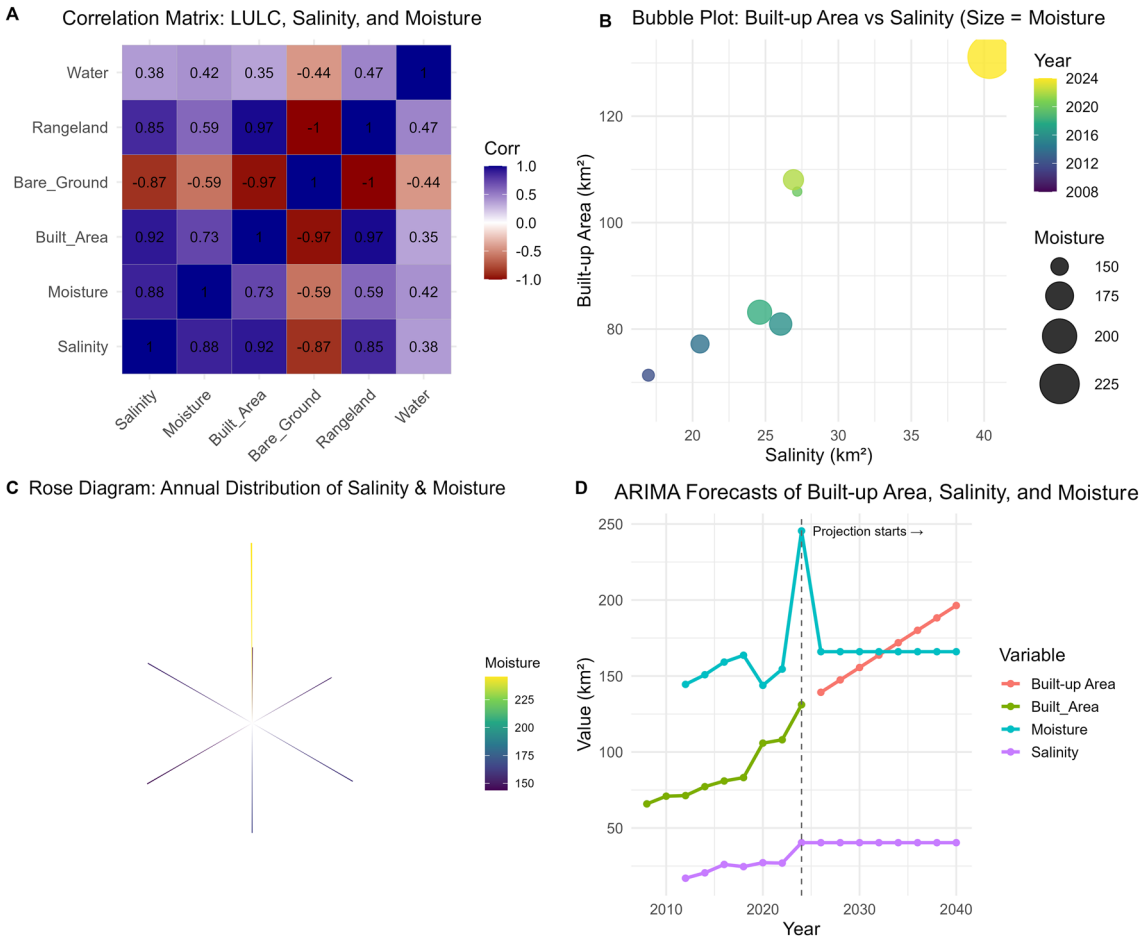

Fig. 26 Coupled relationships and temporal evolution of soil salinity, soil moisture, and land-use/land-cover (LULC) variables, illustrating strong hydro-saline–urbanization linkages, contrasting responses across land-cover types, and consistent long-term trends derived from satellite analysis

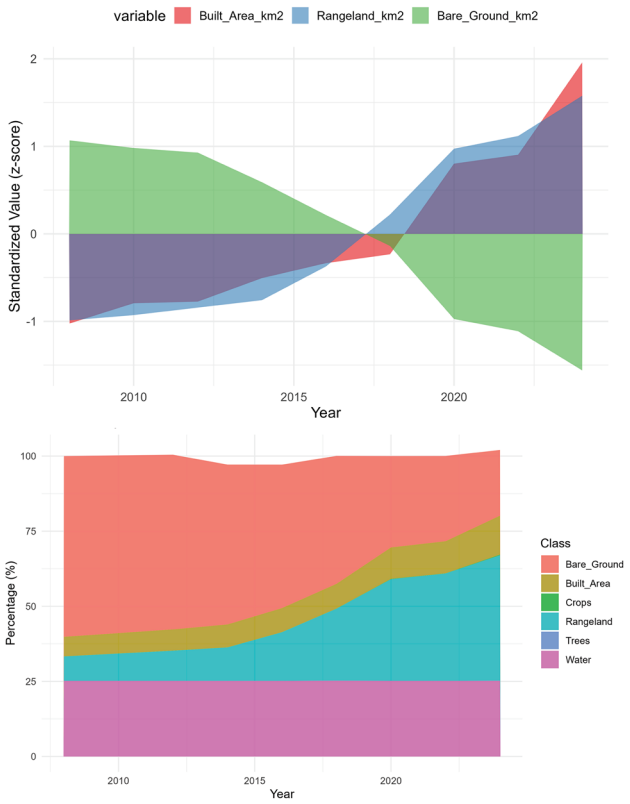

Fig. 27 Deriving trends of LULC changes over time

Appendix D

EC from Resistivity

See Table 13.

Shallow subsurface electrical measurements were conducted using a SAS1000 Terrameter (ABEM Instrument AB, Sweden) with a Schlumberger electrode configuration, in which the current electrodes (A–B) are symmetrically expanded while the potential electrodes (M–N) remain relatively close to the center of the array (Dahlin et al. 2006; Telford et al. 1990). The survey employed a current electrode half-spacing of AB/2 = 1.5 m (total AB = 3.0 m) and a potential electrode half-spacing of MN/2 = 0.5 m (total MN = 1.0 m). In Schlumberger soundings, the depth of investigation is primarily controlled by the current-electrode separation (AB), whereas the potential-electrode spacing mainly affects voltage resolution and measurement sensitivity rather than penetration depth (Loke 2004).

Based on established DC resistivity principles, the effective depth of investigation is typically on the order of 0.1–0.3 times the total current electrode spacing (AB), corresponding in this configuration to an expected penetration depth of approximately 0.3–0.9 m, which is appropriate for characterizing near-surface salinity and moisture conditions (Telford et al. 1990; Loke 2004).

Apparent resistivity values were calculated internally by the SAS1000 Terrameter from field measurements of injected current (I) and resulting potential difference (ΔV). The measured resistance (R) was computed as:

$$R = \frac{\Delta V}{I}$$

The apparent resistivity (ρ_a, Ω·m) was then calculated using the Schlumberger geometric factor (K) according to:

$$\rho_a = K \times R$$

For the Schlumberger array, the geometric factor is defined as:

Table 13 VES data measurements using a SAS1000 resistivity meter used to derive EC in the study area

No	AB/2 (m)	MN/2 (m)	K	R (Ω)	Apparent Resistivity ρa (Ω·m)	Remarks
1	1.5	0.5	6.28E+00	1.16E+00	7.28E+00	Used for EC calculation from 24 VES
2	2.5	0.5	1.88E+01	1.13E−01	2.13E+00	
3	4.0	0.5	4.95E+01	2.00E−02	9.89E−01	
4	6.0	0.5	1.12E+02	7.00E−03	7.86E−01	
5	8.0	0.5	2.00E+02	3.00E−03	6.01E−01	
6	10.0	0.5	3.13E+02	2.00E−03	6.26E−01	
7	12.0	0.5	4.51E+02	1.00E−03	4.51E−01	
8	15.0	0.5	7.06E+02	1.00E−03	7.06E−01	
9	15.0	5.0	6.28E+01	1.10E−02	6.91E−01	
10	20.0	5.0	1.18E+02	6.00E−03	7.07E−01	
11	25.0	5.0	1.88E+02	4.00E−03	7.54E−01	
12	30.0	5.0	2.75E+02	2.00E−03	5.50E−01	
13	30.0	10.0	1.26E+02	6.00E−03	7.54E−01	
14	40.0	10.0	2.36E+02	3.00E−03	7.07E−01	
15	50.0	10.0	3.77E+02	2.00E−03	7.54E−01	
16	60.0	10.0	5.50E+02	1.00E−03	5.50E−01	
17	75.0	10.0	8.67E+02	9.00E−04	7.81E−01	

$$K = \pi \left(\frac{\left(AB/2\right)^2 - \left(MN/2\right)^2}{MN} \right)$$

According to manufacturer specifications and standard geophysical references, the typical uncertainty associated with apparent resistivity measurements using modern terrameters under favorable electrode contact conditions is generally within ± 2–5%, with additional uncertainty potentially arising from electrode contact resistance, shallow subsurface heterogeneity, and cultural noise (Dwamena and Zhou 2026; Telford et al. 1990). These uncertainty levels are acceptable for shallow environmental and hydro-salinity investigations and do not affect the relative interpretation of conductivity patterns derived from the VES data.

Example of Raw Data Used in the Present Study for Calculation Thresholds from EC

Equipment: SAS1000, GPS.
Sounding No.: 24.
Elevation: 1.5 m.
Coordinates: N 19.7477, E 37.25925.
Configuration: Schlumberger.

Acknowledgements The authors gratefully acknowledge the Joint Executive Program between Hungary and Sudan (Stipendium Hungaricum Scholarship) for financial and academic support. The authors also thank the Faculty of Earth Sciences, Department of Geophysics (Assist. Prof. Abdu Elazeem Osman Adam), Red Sea University, for providing the electrical resistivity instruments and previous data used in this study. Additional support for this research was provided by the University of Debrecen Program for Scientific Publication. Furthermore, the authors acknowledge the United States Geological Survey (USGS) for providing access to Landsat imagery and MODIS land-use/land-cover datasets, the European Copernicus Programme for Sentinel-2 data, and the ArcGIS Living Atlas for land-use/land-cover products. These datasets were essential for the spatial and temporal analyses conducted in this study. The authors also sincerely thank the anonymous reviewers for their constructive comments and valuable suggestions, which significantly improved the quality and clarity of the manuscript. The authors are grateful to Dr. Richard William McIntosh for his professional English-language review and contributions to improving the clarity and consistency of the manuscript.

Author Contributions All authors contributed to the study conception and design. Abazar M. A. Daoud and Péter Rózsa performed material preparation, data collection, validation, software, methodology, investigation, and conceptualization. Abazar M. A. Daoud wrote the first draft of the manuscript. Péter Rózsa (Writing – review & editing, visualization, validation, supervision, and conceptualization.). Novák Tibor József reviewed the entire manuscript. Mahmoud M. Kazem contributed to data curation and analysis. All authors commented on previous versions of the manuscript. All authors read and approved the final manuscript.

Funding Open access funding provided by University of Debrecen. This research did not receive any specific grant from funding agencies in the public, commercial, or not-for-profit sectors.

Data Availability All data supporting the findings of this study are available in the supplementary files accompanying this article.

Declarations

Generative AI Use During the preparation of this work, the authors used (ChatGPT 5.2 / OpenAI) in order to generate codes for R language, and to enhance readability. After using this tool/service, the authors reviewed and edited the content as needed and take full responsibility for the content of the published article.

Conflict of Interest The authors declare that they have no known competing financial interests or personal relationships that could have appeared to influence the work reported in this paper.

References

Abd El-Hamid HT, Alshehri F, El-Zeiny AM, Nour-Eldin H (2023) Remote sensing and statistical analyses for exploration and prediction of soil salinity in a vulnerable area to seawater intrusion. Mar Pollut Bull 187:114555. https://doi.org/10.1016/j.marpolbul.2022.114555

Abdelbagi YFA, Mohamed BOO (2024) Towards Integrated and Sustainable Water Management in Water-scarce Arid Environments: Case of Sudan. IntechOpen, In Hydrology - Current Research and Future Directions. https://doi.org/10.5772/intechopen.1004717

Abuelgasim A, Ammad R (2019) Mapping soil salinity in arid and semi-arid regions using Landsat 8 OLI satellite data. Remote Sens Appl Soc Environ 13:415–425. https://doi.org/10.1016/j.rsase.2018.12.010

Akça E, Aydin M, Kapur S, Kume T, Nagano T, Watanabe T, Çilek A, Zorlu K (2020) Long-term monitoring of soil salinity in a semi-arid environment of Turkey. CATENA 193:104614. https://doi.org/10.1016/j.catena.2020.104614

Al-Imam OA, Elsayed Zeinelabdein KA, M Elsheikh AE (2015) Stratigraphy and subsurface weathering grade in determination of foundation properties in the area between Port-Sudan and Suakin, Red Sea Region, NE Sudan. Am J Earth Sci 2(4):71–77

Avdan U, Jovanovska G (2016) Algorithm for automated mapping of land surface temperature using Landsat 8 satellite data. J Sensors 2016:1–8. https://doi.org/10.1155/2016/1480307

Bai L, Long D, Yan L (2019) Estimation of surface soil moisture with downscaled land surface temperatures using a data fusion approach for heterogeneous agricultural land. Water Resour Res 55(2):1105–1128. https://doi.org/10.1029/2018WR024162

Bannari A, El-Battay A, Bannari R, Rhinane H (2018) Sentinel-MSI VNIR and SWIR bands sensitivity analysis for soil salinity discrimination in an arid landscape. Remote Sens 10(6):855. https://doi.org/10.3390/rs10060855

Bashar T, Uddin MZ (2025) Effects of land use change on surface runoff and infiltration: the case of Dhaka City. Urban Sci 9(12):497. https://doi.org/10.3390/urbansci9120497

Bhardwaj AK, Mishra VK, Singh AK, Arora S, Srivastava S, Singh YP, Sharma DK (2019) Soil salinity and land use-land cover interactions with soil carbon in a salt-affected irrigation canal command of Indo-Gangetic Plain. CATENA 180:392–400. https://doi.org/10.1016/j.catena.2019.05.015

Boutin J, Yueh S, Bindlish R, Chan S, Entekhabi D, Kerr Y, Kolodziejczyk N, Lee T, Reul N, Zribi M (2023) Soil moisture and sea surface salinity derived from satellite-borne sensors. Surv Geophys 44(5):1449–1487. https://doi.org/10.1007/s10712-023-09798-5

Brakman S, Kohl T, van Marrewijk C (2025) World population and trade in the 21st century. Rev Int Econ 33(2):486–501. https://doi.org/10.1111/roie.12782

Andrea Cattarossi, Paolo Polo, Paolo Mastrocola, Elmusalami Fadlallah, Sami Ouechtati, Giovanni Isotton, Alessio Fileccia, Casey Walther (2019) Management of Critical Water Supply Sources near Port Sudan, Sudan : Arbaat Dam and Well Fields at Arbaat and Moj. http://documents.worldbank.org/curated/en/650011609914976904

Chaaou A, Ait-Ichou H, El Hachemy S, Chikhaoui M, Naimi M, Hssaisoune M, El Hafyani M, Ait Brahim Y, Bouchaou L (2025) Mapping soil salinity using machine learning and remote sensing data in semi-arid croplands. Front Soil Sci. https://doi.org/10.3389/fsoil.2025.1653400

Chen H-P, Jiang Y, Markou G (2022) Structural performance deterioration of corroding reinforced concrete columns in marine environments. Ocean Eng 262:112155. https://doi.org/10.1016/j.oceaneng.2022.112155

Cover ML, Change LC (1999) MODIS land cover product algorithm theoretical basis document (ATBD) version 5.0. MODIS Documentation, pp 42–47

Dahlin T, Zhou B (2006) Multiple-gradient array measurements for multichannel 2D resistivity imaging. Near Surf Geophys 4(2):113–123. https://doi.org/10.3997/1873-0604.2005037

Daoud AMA, Abir MNAM, Kazem MM, Satti AMN, Shebl A, Mohamed MAA, Agyemfra GJ, Elrasheed AA, Csámer Á, Rózsa P (2025) Comprehensive hazard susceptibility assessment in Port Sudan city using AHP: emphasizing flash flood risk, soil moisture, and salinity dynamics. Geomat Nat Hazards Risk. https://doi.org/10.1080/19475705.2025.2593297

Dey R, Matin A, Lewark E, Faruk T, Bin Bachinin A, Leuthold S, Cotrufo MF, Pallickara S, Pallickara SL (2025) DeepSalt: Bridging Laboratory and Satellite Spectra through Domain Adaptation and Knowledge Distillation for Large-Scale Soil Salinity Estimation. ArXiv Preprint ArXiv:2510.23124

Dinnat EP, Le Vine DM, Boutin J, Meissner T, Lagerloef G (2019) Remote sensing of sea surface salinity: comparison of satellite and in situ observations and impact of retrieval parameters. Remote Sens 11(7):750. https://doi.org/10.3390/rs11070750

Dwamena GF, Mensah BE (2026) Diagnostic and Recovery Method for Boot Failure in PC/104-Based Geophysical Resistivity Instruments Following CMOS Configuration Loss: On the ABEM Terrameter SAS-1000/4000 Using the PFM-540I Platform. EGUsphere [Preprint]. https://doi.org/10.5194/egusphere-2025-6396

Elena C, Chiara P, Gianni B, Alessandra M (2024) Corrosion attack in existing reinforced concrete structures: in-field investigation and analysis of naturally corroded bars. Mater Struct 57(10):243. https://doi.org/10.1617/s11527-024-02477-w

Elhag M (2016) Evaluation of different soil salinity mapping using remote sensing techniques in arid ecosystems, Saudi Arabia. J Sens. https://doi.org/10.1155/2016/7596175

Elsawy MBD, Lakhouit A (2020) A review on the impact of salinity on foundation soil of coastal infrastructures and its implications to north of Red Sea coastal constructions. Arab J Geosci 13(13):555. https://doi.org/10.1007/s12517-020-05601-6

Elsheikh AEM, Elsayed ZKA (2015) Sea water/fresh water interaction in the Red Sea coast around Port-Sudan town-Red Sea State-Eastern Sudan. Nile Water Sci Eng J 8(1):67–73

Eswar D, Karuppusamy R, Chellamuthu S (2021) Drivers of soil salinity and their correlation with climate change. Curr Opin Environ Sustain 50:310–318. https://doi.org/10.1016/j.cosust.2020.10.015

Eyankware MO, Mba-Otike MN, Odesa GE, Chukwusa FO, Osisanya WO, Eyankware-Ulakpa RO, Akakuru OC, Komolafe NP (2025) Saline intrusion in Niger Delta coastal aquifers, drivers, hydrogeological dynamics and mitigation strategies. Discov Geosci 3(1):150. https://doi.org/10.1007/s44288-025-00264-w

Gad MME-S, Mohamed MHA, Mohamed MR (2021) Soil salinity mapping using remote sensing and GIS. Geomatica 75(4):1–15. https://doi.org/10.1139/geomat-2021-0015

Gao Z, Li X, Zuo L, Zou B, Wang B, Wang WJ (2025) Unveiling soil salinity patterns in soda saline-alkali regions using Sentinel-2 and SDGSAT-1 thermal infrared data. Remote Sens Environ 322:114708. https://doi.org/10.1016/j.rse.2025.114708

Gökçe HS (2024) Durability of slag-based alkali-activated materials: a critical review. J Aust Ceram Soc 60(3):885–903. https://doi.org/10.1007/s41779-024-01011-z

Hagage M, Abdulaziz AM, Elbeih SF, Hewaidy AGA (2024) Monitoring soil salinization and waterlogging in the northeastern Nile Delta linked to shallow saline groundwater and irrigation water quality. Sci Rep 14(1):27838. https://doi.org/10.1038/s41598-024-77954-x

Harris I, Osborn TJ, Jones P, Lister D (2020) Version 4 of the CRU TS monthly high-resolution gridded multivariate climate dataset. Sci Data 7(1):109. https://doi.org/10.1038/s41597-020-0453-3

Hasoba AMM, Yasin EHE, Osman MBO, Czimber K (2025) Monitoring Ecosystem Dynamics Using Machine Learning: Random Forest-Based LULC Analysis in Dinder Biosphere Reserve, Sudan. The 1st International Conference on Advanced Remote Sensing – Shaping Sustainable Global Landscapes (ICARS 2025). 2. https://doi.org/10.3390/engproc2025094002

Hassani A, Azapagic A, Shokri N (2020) Predicting long-term dynamics of soil salinity and sodicity on a global scale. Proc Natl Acad Sci 117(52):33017–33027. https://doi.org/10.1073/pnas.2013771117

Hawash E, El-Hassanin A, Amer W, El-Nahry A, Effat H (2021) Change detection and urban expansion of Port Sudan, Red Sea, using remote sensing and GIS. Envir Monit Assessment. https://doi.org/10.1007/s10661-021-09486-0

Heiss JW, Mase B, Shen C (2022) Effects of Future increases in tidal flooding on salinity and groundwater dynamics in coastal aquifers. Water Res Res. https://doi.org/10.1029/2022WR033195

Hou J, Rusuli Y (2022) Assessment of soil salinization risk by Remote Sensing-Based Ecological Index (RSEI) in the Bosten Lake Watershed, Xinjiang in Northwest China. Sustain 14(12):7118. https://doi.org/10.3390/su14127118

Hyndman R, Athanasopoulos G, O'Hara-Wild M, Palihawadana N, Wickramasuriya S, Hyndman MR (2025) Package 'fpp3'

Jamali AA, Montazeri Naeeni MA, Zarei G (2020) Assessing the expansion of saline lands through vegetation and wetland loss using remote sensing and GIS. Remote Sens Appl Soc Environ 20:100428. https://doi.org/10.1016/j.rsase.2020.100428

Kheiralla, K. M., & Al-Imam, O. A. O. (2013). Engineering Geophysical Study for Geotechnical Investigation, Port Sudan, Red Sea, Sudan. *International Journal of Geology, Agriculture and Environmental Sciences*, *1*(1), 26–31. www.woarjournals.org/IJGAES

Klein N, Gómez ED, Duffó GS, Farina SB (2022) Effect of sulphate on the corrosion of reinforcing steel in concrete. Constr Build Mater 354:129214. https://doi.org/10.1016/j.conbuildmat.2022.129214

Lekka C, Detsikas SE, Petropoulos GP, Chalkias C (2024) Mapping and monitoring of salt-affected soils: the contribution of geoinformation. Remote Sens Precision Agric. https://doi.org/10.1016/B978-0-323-91068-2.00016-3

Li A, Wu Y, Cao S (2024) Effects of land use-land cover on soil water and salinity contents. Eco Front 44(2):307–314. https://doi.org/10.1016/j.chnaes.2023.07.002

Liuzzo L, Puleo V, Nizza S, Freni G (2020) Parameterization of a Bayesian Normalized Difference Water Index for surface water detection. Geosci 10(7):260. https://doi.org/10.3390/geosciences10070260

Loke MH (2004) Tutorial: 2-D and 3-D electrical imaging surveys

Lorrain-Soligon L, Robin F, Bertin X, Jankovic M, Rousseau P, Lelong V, Brischoux F (2023) Long-term trends of salinity in coastal wetlands: effects of climate, extreme weather events, and sea water level. Environ Res 237:116937. https://doi.org/10.1016/j.envres.2023.116937

Mandal UK, Ghosh A, Karim F, Mallick S, Nayak DB, Bhutia RN, Bhardwaj AK, Lama TD, Burman D, Choudhury P, Mahanta KK, Raut S, Mandal S, Mainuddin M (2025) Land use change and soil salinization in the Sundarbans: a machine-learning based analysis of long-term transformation and future projections. Environ Monit Assess 197(12):1380. https://doi.org/10.1007/s10661-025-14829-2

Masoud AA, Koike K, Atwia MG, El-Horiny MM, Gemail KS (2019) Mapping soil salinity using spectral mixture analysis of landsat 8 OLI images to identify factors influencing salinization in an arid region. Int J Appl Earth Obs Geoinf 83:101944. https://doi.org/10.1016/j.jag.2019.101944

Mazhar S, Pellegrini E, Contin M, Bravo C, De Nobili M (2022) Impacts of salinization caused by sea level rise on the biological processes of coastal soils - A review. Front Envir Sci. https://doi.org/10.3389/fenvs.2022.909415

Meng G, Zhu G, Jiao Y, Qiu D, Wang Y, Lu S, Li R, Liu J, Chen L, Wang Q, Huang E, Li W (2025) Soil salinity patterns reveal changes in the water cycle of inland river basins in arid zones. Hydrol Earth Syst Sci 29(19):5049–5063. https://doi.org/10.5194/hess-29-5049-2025

Metternicht GI, Zinck JA (2003) Remote sensing of soil salinity: potentials and constraints. Remote Sens Environ 85(1):1–20. https://doi.org/10.1016/S0034-4257(02)00188-8

Morshed MdM, Islam MdT, Jamil R (2016) Soil salinity detection from satellite image analysis: an integrated approach of salinity indices and field data. Environ Monit Assess 188(2):119. https://doi.org/10.1007/s10661-015-5045-x

National Oceanic and Atmospheric Administration. (2025) Weather. National Oceanic and Atmospheric Administration. https://www.noaa.gov/weather

Nguyen DN, Chiapponi E, Nguyen DM, Antonellini M, Silvestri S (2024) Detection and mitigation of soil salinization risk from saline/brackish water aquaculture in coastal areas: an application of remote sensing and managed aquifer recharge. J Coast Conserv 28(5):68. https://doi.org/10.1007/s11852-024-01067-w

Niclòs R, Puchades J, Coll C, Barberà MJ, Pérez-Planells L, Valiente JA, Sánchez JM (2021) Evaluation of Landsat-8 TIRS data recalibrations and land surface temperature split-window algorithms over a homogeneous crop area with different phenological land covers. ISPRS J Photogramm Remote Sens 174:237–253. https://doi.org/10.1016/j.isprsjprs.2021.02.005

Peters R, Reis ÂCA, Mehlig U, Wimmler M-C, Vollhüter J, Pimple U, Tietjen B, Berger U (2025) Modelling the dynamics of soil moisture and soil water salinity in tropical saltmarshes. Ecol Model 504:111089. https://doi.org/10.1016/j.ecolmodel.2025.111089

Platonov A, Noble A, Kuziev R (2013) Soil Salinity Mapping Using Multi-Temporal Satellite Images in Agricultural Fields of Syrdarya Province of Uzbekistan. In Developments in Soil Salinity Assessment and Reclamation, Springer, Netherlands. https://doi.org/10.1007/978-94-007-5684-7_5

Reul N, Grodsky SA, Arias M, Boutin J, Catany R, Chapron B, D'Amico F, Dinnat E, Donlon C, Fore A, Fournier S, Guimbard S, Hasson A, Kolodziejczyk N, Lagerloef G, Lee T, Le Vine DM, Lindstrom E, Maes C, Yueh S (2020) Sea surface salinity estimates from spaceborne L-band radiometers: An overview of the first decade of observation (2010–2019). Remote Sens Envir. https://doi.org/10.1016/j.rse.2020.111769

Rijniers LA, Pel L, Huinink HP, Kopinga K (2005) Salt crystallization as damage mechanism in porous building materials—a nuclear magnetic resonance study. Magn Reson Imaging 23(2):273–276. https://doi.org/10.1016/j.mri.2004.11.023

Saad K, Kallel A, Castaldi F, Sahli Chahed T (2024) Soil salinity detection and mapping by multi-temporal Landsat data: Zaghouan case study (Tunisia). Remote Sens 16(24):4761. https://doi.org/10.3390/rs16244761

Sahbeni G, Ngabire M, Musyimi PK, Székely B (2023) Challenges and opportunities in remote sensing for soil salinization mapping and monitoring: a review. Remote Sens 15(10):2540. https://doi.org/10.3390/rs15102540

Salem OH, Jia Z (2024) Evaluation of different soil salinity indices using remote sensing techniques in Siwa Oasis, Egypt. Agronomy 14(4):723. https://doi.org/10.3390/agronomy14040723

Saxena S, Baghban MH (2023) Seawater concrete: a critical review and future prospects. Dev Built Environ 16:100257. https://doi.org/10.1016/j.dibe.2023.100257

Sharma M, Bangotra P, Gautam AS, Gautam S (2022) Sensitivity of normalized difference vegetation index (NDVI) to land surface temperature, soil moisture and precipitation over district Gautam Buddh Nagar, UP, India. Stoch Environ Res Risk Assess 36(6):1779–1789. https://doi.org/10.1007/s00477-021-02066-1

Siddig MMS, Sauer D, Brevik EC (2025) Quantitative soil mapping in Sudan−a systematic review. Geoderma Reg 42:e00990. https://doi.org/10.1016/j.geodrs.2025

Su Q, Kambale RD, Tzeng J-H, Amy GL, Ladner DA, Karthikeyan R (2025) The growing trend of saltwater intrusion and its impact on coastal agriculture: Challenges and opportunities. Sci Total Envir. https://doi.org/10.1016/j.scitotenv.2025.178701

Taha ATB, Ebaid GS, Aboul-Atta N (2015) Surface water study in eastern part of Sudan (Khor Arbaat case study). Civ Eng Res Mag 37(3):210–230

Tarolli P, Luo J, Park E, Barcaccia G, Masin R (2024) Soil salinization in agriculture: mitigation and adaptation strategies combining nature-based solutions and bioengineering. iSci 27(2):108830. https://doi.org/10.1016/j.isci.2024.108830

Team RC (2024) R: A language and environment for statistical computing. R Foundation for Statistical Computing, Wien, Itävalta

Telford WM, Geldart LP, Sheriff RE (1990) Applied geophysics. Cambridge University Press

Thiam S, Villamor GB, Faye LC, Sène JHB, Diwediga B, Kyei-Baffour N (2021) Monitoring land use and soil salinity changes in coastal landscape: a case study from Senegal. Environ Monit Assess 193(5):259. https://doi.org/10.1007/s10661-021-08958-7

Vanhellemont Q (2020) Combined land surface emissivity and temperature estimation from Landsat 8 OLI and TIRS. ISPRS J Photogramm Remote Sens 166:390–402. https://doi.org/10.1016/j.isprsjprs.2020.06.007

Vergès-Belmin V (2008) Illustrated glossary on stone deterioration patterns. Icomos

Wang J, Wang W, Hu Y, Tian S, Liu D (2021) Soil moisture and salinity inversion based on new remote sensing index and neural network at a salina-alkaline wetland. Water Basel 13(19):2762. https://doi.org/10.3390/w13192762

Wang E, Zhang H, Wang J, Cao W, Li D (2025) Simulation and sensitivity analysis of remote sensing reflectance for optically shallow

water bathymetry. Remote Sens 17(8):1384. https://doi.org/10.3390/rs17081384

Weng Q (2012) Remote sensing of impervious surfaces in the urban areas: requirements, methods, and trends. Remote Sens Environ 117:34–49. https://doi.org/10.1016/j.rse.2011.02.030

Wijerathne D, Samarasekara RSM, Satanarachchi N, Vithanage M, Lakmal HMA (2025) Evaluating the environmental impacts of hard coastal engineering structures on groundwater salinity and salinity intrusion: insights from the Marawila Coastal Zone, Sri Lanka. Environ Chall 19:101145. https://doi.org/10.1016/j.envc.2025.101145

Yang B, Hu X, Li A, Zhao T, Sun Y, Fu H (2025) Degradation mechanism of cast-in-situ concrete under long-term sulfate saline soil attack. Constr Build Mater 478:141401. https://doi.org/10.1016/j.conbuildmat.2025.141401

Zeyada MA, Al-Gaadi AK, Tola E, Madugundu R, Alameen AA (2023) Sentinel-2 satellite imagery application to monitor soil salinity and calcium carbonate contents in agricultural fields. Phyton 92(5):1603–1620. https://doi.org/10.32604/phyton.2023.027267

Zhang X, Zuo Y, Wang T, Han Q (2024) Salinity effects on soil structure and hydraulic properties: implications for pedotransfer functions in coastal areas. Land Basel 13(12):2077. https://doi.org/10.3390/land13122077